

Multiscale Spatial Patterns in Giant Dike Swarms Identified through Objective Feature Extraction

A. Kubo Hutchison¹, L. Karlstrom¹, T. Mittal²

¹Department of Earth Sciences, 1272 University of Oregon, Eugene, Oregon 97403, USA

²Department of Geosciences, 503 Deike Building, University Park, PA 16802

Key Points:

- Superimposed spatial patterns in dike swarms are revealed by the Hough Transform
- Deccan Traps and Columbia River Flood Basalts exhibit multiscale overlapping dike swarm structures
- Linear and radial mesoscale swarm structures are identifiable in Hough space

Corresponding author: Allison Kubo Hutchison, akubo@uoregon.edu

Abstract

Dike swarms are ubiquitous on terrestrial planets and represent the frozen remnants of magma transport networks. However, spatial complexity, protracted emplacement history, and uneven surface exposure typically make it difficult to quantify patterns in dike swarms on different scales. In this study, we address this challenge using the Hough Transform to objectively link dissected dike segments and analyze multiscale spatial structure in dike swarms. We apply this method to swarms of three scales: the Spanish Peaks, USA; the Columbia River Flood Basalt Group (CRBG), USA; the Deccan Traps Flood Basalts, India. First, we cluster dike segments in Hough Transform space, recognizing prevalent linearly aligned structures that represent single dikes or dike packets, with lengths up to 10–30 x the mapped mean segment length. Second, we identify colinear and radial dike segment mesoscale structures within each data set, using the Hough Transform to segment swarms into constituent spatial patterns. We show that for both the CRBG and Deccan Traps, a single radial swarm does not well characterize the data. Instead, multiple and sometimes overlapping mesoscale linear and radial features are prevalent. This suggests a time-evolving transport network where structural inheritance of dike pathways over an extended time is likely common, but large-scale reorganizations of the plumbing system that imply state shifts in crustal stresses or mantle melt supply also occur. We expect that the Hough Transform may find useful applications in a variety of geologic settings where many quasi-linear features, at any scale, are superimposed spatially.

Plain Language Summary

Dikes act as pipelines to transport magma from the deep Earth to the surface where it can erupt. Some of the largest concentrations of dikes on Earth occur in ancient continental flood basalts (CFBs), areas of massive volcanic output, but the spatial complexity and scale of these dike swarms has been a barrier to understanding the patterns within. We develop a new method to characterize distributions of linear features, such as dike swarms, inspired by tools and algorithms from image processing. We apply this tool to two CFBs, the Columbia River Flood Basalt Group, USA, and the Deccan Traps, India, as well as a smaller swarm in the Spanish Peaks, USA. We find numerous small packets of aligned segments and larger, radial, and linear patterns of dikes. Objective identification of these structures should provide a new quantitative basis for understanding how magma is transported over time.

1 Introduction

Dikes are a primary method of magma transport in the crust, connecting deep mantle melting with crustal magma storage zones and sometimes surface eruptions (Rivalta et al., 2015; Gonnermann & Taisne, 2015). Dikes are sometimes known to spatially focus into areas of high dike activity known as dike swarms across a variety of scales. Dike swarms are multiscale phenomena which range in scale from a single edifice such as the Spanish Peaks (kilometer scale) (Odé, 1957; Muller & Pollard, 1977) to continental scale such as the Mackenzie Swarm ($> 1000\text{km}$) (Fahrig & Jones, 1969; Baragar et al., 1996). On Earth, giant dike swarms are usually associated with anomalous mantle melting events that result in Large Igneous Provinces (LIPs), tectonic breakups, and thus record significant magmatic-tectonic events in Earth's history (Yale & Carpenter, 1998; Bond & Wignall, 2014; Ernst et al., 2021). Although instances of dike swarm injection have been observed in recent times (Ayele et al., 2007), we have never observed an emplacement of a dike swarm of the scale that is often seen in the rock record especially in the case of continental flood basalts (CFBs) (Bunger et al., 2013, 2012). Dike swarms have also been observed or inferred on other planets such as Mars, Venus and Mercury, indicating that these features are essential to the movement of magma in a terrestrial planetary body (Ernst et al., 2001; Grosfils & Head, 1994; Crane & Bohanon, 2021; Rivas-Dorado et al., 2022). Dike swarms represent one of the most visually striking illustration of long-distance (10s of km scale) vertical and lateral magma transport from crustal magma reservoirs.

Field studies of exhumed dike swarms have provided insight into their dynamics and complexities at a range of scales (Morriss et al., 2020; Jolly & Sanderson, 1995; Ray et al., 2007; Paquet et al., 2007). Dike segment thickness varies from centimeter scale to 100s of meters while lengths vary from mere meters to 100s of kilometers. In the largest end of the spectrum, CFB dikes have been observed to be over 100 m wide and kilometers to 100s of kilometers long, considerably larger than dikes associated with Ocean Islands or arc settings (Karlstrom et al., 2017; Thiele et al., 2020; Morriss et al., 2020; Mittal et al., 2021). Dike widths have been proposed to follow power-law distributions (Gudmundsson, 1995) although there is continued debate over whether log-normal or Weibull distributions may provide better fits considering issues with sampling the smallest scale of igneous dikes (Krumbholz et al., 2014; Jolly & Sanderson, 1995; Glazner & Mills, 2012).

76 Dike width and its distribution have been proposed to be controlled by magmatic
77 overpressure (Babiker & Gudmundsson, 2004; Gudmundsson, 2002), host rock rheology
78 (Karlstrom et al., 2017; Krumbholz et al., 2014), and depth of emplacement (Delaney
79 et al., 1986). Some of these theoretical and field-based inferences have been tested by
80 laboratory analog studies (J. L. Kavanagh et al., 2018, 2006). These studies have high-
81 lighted the critical role of crustal layering (both rigidity and density layering), topographic
82 stresses, magma buoyancy, and magma inflow rate in controlling the spatial pattern of
83 dike propagation (e.g., vertical vs. lateral propagation) (J. L. Kavanagh et al., 2015; Ur-
84 bani et al., 2018). Despite uncertainties about how well single dike models extrapolate
85 to large dike swarms with complex inter-dike interaction (Gunaydin et al., 2021), dike
86 swarms have been widely interpreted in terms of paleostresses and as direct evidence of
87 a transcrustal magma plumbing system (Rivalta et al., 2015; Mittal et al., 2021).

88 Remote sensing studies and field mapping (when possible) have led to structural
89 classifications of the largest scale structure of dike swarms (Ernst et al., 2001). Some dike
90 swarms form large radial or fanning structures from a localized center, while others are
91 primarily linear bundles of subparallel segments. These two end members, which we will
92 also focus on in this work, have largely been interpreted as representing two magmatic
93 ‘states’: (a) the stresses are primarily endogenous to the magmatic system (e.g., a plume
94 head (Ernst et al., 1995; Baragar et al., 1996; Mège & Korme, 2004), magma chamber
95 (Callot et al., 2001), or volcanic edifice (Roman & Jaupart, 2014; Acocella & Neri, 2009;
96 Gudmundsson, 2006)) and (b) stresses are imposed exogenously (e.g., tectonic stresses
97 such as rifting (John et al., 2000)). Interpreted this way, the structure of dike swarms
98 can illuminate the mechanism and driving forces of their emplacement (Mège & Korme,
99 2004), and provide a key tool for understanding the links between mantle melting, sur-
100 face volcanism, tectonic rifting, and the Large Igneous Province (LIP) life cycle (Black
101 et al., 2021).

102 Although it is clear that multiscale patterns exist in giant dike swarms, even in-
103 dividual dikes are often dissected into individual segments due to erosion, topography,
104 or exposure. This severely limits the cases where we can directly infer the mesoscale (10-
105 100 kms) and large scale structure (> 100 kms) of dike swarms in a statistically robust
106 manner from observations. For example, based on scaling analysis of Linear Elastic Frac-
107 ture Mechanics (LEFM), dike segments in many databases are much shorter than pre-
108 dicted (Morriss et al., 2020). At present, it is unclear if this mismatch is telling us some-

109 thing about the underlying magma transfer processes or is just a consequence of obser-
110 vational limitations. *In this study, we address this challenge by developing a novel method*
111 *to objectively link dissected segments and utilize tools from image processing to analyze*
112 *mesoscale and large scale structure in dike swarms.*

113 To demonstrate the methods, we first study dikes of the Spanish Peaks region in
114 Colorado, USA – an often cited example of small radial dike swarm – and then focus on
115 the two large LIP dike datasets: dikes of the Columbia River Flood Basalt Group (CRBG)
116 and Deccan Traps Flood Basalts. We focus our analysis primarily on these two systems
117 due to the large scale, amount of overlapping dike orientations, and generally complex
118 spatial patterns of dike segments. These two CFBs also represent some of the best stud-
119 ied LIPs in the context of volcanic stratigraphy, geochronology, and magmatic processes
120 (e.g. V. Camp et al., 2017; Kasbohm & Schoene, 2018; Mittal et al., 2021)

121 We will focus on the following questions:

- 122 1. Do dike swarms mapped as distributions of many disconnected segments actually
123 represent a smaller set of structurally continuous structures?
- 124 2. Are LIP dikes organized into coherent spatial patterns at a sub-swarm or swarm
125 scale?
- 126 3. Do multiscale dike structures differ between the CRBG and Deccan Traps, and
127 if so does this imply differences in emplacement mechanics?

128 To investigate these questions, we have developed a workflow for linking and clus-
129 tering dike segments based on the Hough Transform, an algorithm commonly used in im-
130 age processing (Hough, 1962; Duda & Hart, 1972; Ballard, 1981). We then use Agglom-
131 erative Clustering to classify mesoscale groupings of dike segments in the Hough space
132 (Everitt, 1980; SNEATH, 1957). We show that this method increases the lengths of dike
133 segments by up to 3 orders of magnitude and thus likely better represents the true scale
134 of dikes in geologic data.

135 **2 Methods**

136 **2.1 Hough Transform**

137 The Hough transform (HT) is a feature extraction method extensively used in im-
138 age analysis and computer vision (Hough, 1962; Duda & Hart, 1972). Originally designed

139 to detect lines in images, the algorithm has been adapted to detect arbitrary shapes (Ballard,
 140 1981). Although magmatic dikes are typically linear, they can curve as they propagate
 141 through different stress fields and thus depend on the length scale of the stress fields (Davis
 142 et al., 2021; Acocella & Neri, 2009). To illustrate the method, we will focus primarily
 143 on straight features in the present study and will not link dikes that curve along their
 144 length. Curving dike segments are removed in a preprocessing step before linking (due
 145 to the linearity filter). In practice, a majority of the LIP dikes are linear segments, and
 146 our choice does not strongly affect the overall results. A full extension to curved features
 147 is beyond the scope of the present study.

148 We use the Hough transform to help accomplish two goals: first, to link short dike
 149 segments into longer dikes; and second to evaluate the mesoscale structure of the dike
 150 swarm. The Hough Transform is independent of Cartesian midpoint location allowing
 151 us to link dike segments together that are far away from each other. In the classic HT
 152 formulation, initially an edge detection method is applied to an image to find disconti-
 153 nuities that may constitute shapes or features (Ziou & Tabbone, 1998). Each edge point
 154 is then transformed according to the following equation (Duda & Hart, 1972):

$$155 \quad \rho = x \cos \theta + y \sin \theta \quad (1)$$

156 where θ is angle from the x axis in counterclockwise direction, and ρ is the distance of
 157 a ray from the origin to the line defined by the point and θ . *Lines in Cartesian space*
 158 *become points in Hough space (HS); points in Cartesian space are curves in Hough space*
 159 *(Figure 1)*. All the image edge points in Hough space (or a subset of them) are summed
 160 to form the accumulator array, which then votes on the most likely lines - the most rep-
 161 resented values of ρ and θ .

162 In the application here, we use dike segment maps derived from field mapping and
 163 remote sensing as data inputs. Each dike segment is pre-defined between two endpoints.
 164 Thus, we skip the edge detection and accumulator array steps. *We assume that dikes*
 165 *all represent straight lines (ignoring curving dike segments) and thus each dike segment*
 166 *is represented by a single point in the Hough space regardless of its length*. For each dike
 167 segment in Cartesian space, we determine the angle (θ) using :

$$168 \quad \theta = \tan^{-1} \left(\frac{x_2 - x_1}{y_1 - y_2} \right) = \tan^{-1} \left(-\frac{1}{m} \right) \quad (2)$$

169 where the dike segment is represented by its endpoints (x_i) and (y_i) $i = 1, 2$ and m is
 170 the slope of the line. Angle, measured in degrees, varies between -90° and 90° . The neg-

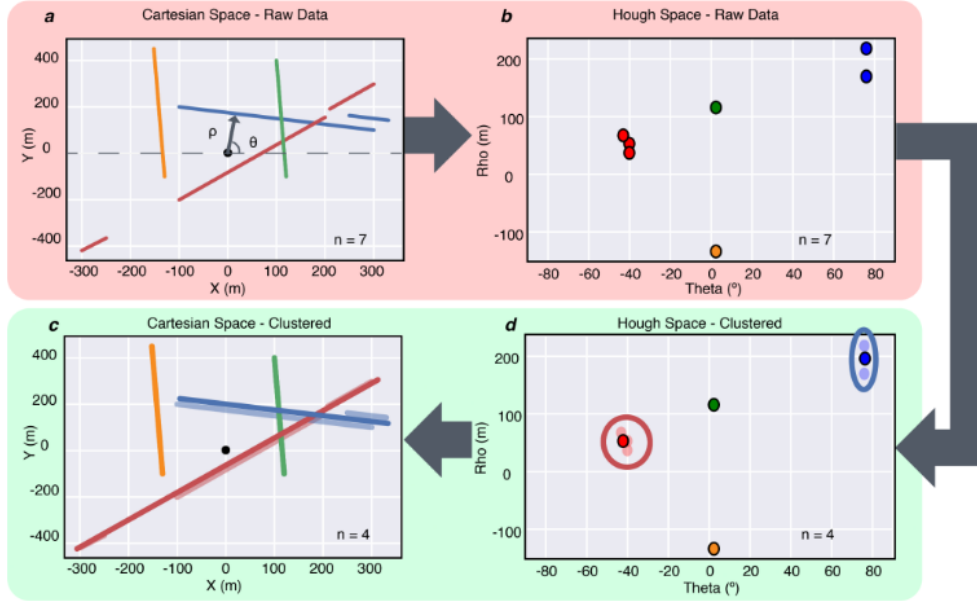


Figure 1. Dike linking algorithm using the Hough Transform. First, raw data in Cartesian space are converted into Hough space **A-B**. Agglomerative clustering is then performed on the data in Hough coordinates (**D**), in this example there are four dikes total and two (red and blue) clusters. The clusters are redrawn by connecting the endpoints of the segments in the cluster.

171 ative angles represent clockwise rotation from vertical (e.g., red line in Figure 1a) and
 172 the positive angles represent anticlockwise rotation (e.g., blue line in Figure 1a). An Hough
 173 angle of 0° represents a feature with North-South orientation or azimuthal bearing of
 174 360° . Angles of -90° and 90° are equivalent representing a line of slope equal to zero
 175 or lineament oriented East-West. The perpendicular distance (ρ) is measured from a spec-
 176 ified origin location and is calculated as

$$177 \quad \rho = (-m(x_1 - x_c) + y_1) \sin(\theta) = b \sin(\theta) \quad (3)$$

178 where b is the y-intercept of the line and either end point can be used to calculate ρ . The
 179 perpendicular distance ρ is measured in units of length and can be both positive and neg-
 180 ative. Positive ρ indicates an intersection point to the right of the chosen Hough trans-
 181 form origin (e.g., red line in Figure 1 a), while a negative distance indicates an intersec-
 182 tion to the left of the origin (e.g., orange line in Figure 1a).

183 An important part of our method is to choose an appropriate origin for the Hough
 184 transform, (x_c, y_c) . The choice of origin does have an effect on the resulting Hough space

185 and the resulting clustering. By default we set the center of transform to be the aver-
186 age of the midpoints of the dike segments. We have extensively experimented with how
187 the choice of origin affects the final results and found that our default choice produces
188 physically reasonable results.

189 **2.2 Clustering Dike Segments**

190 To link dike segments, we apply Agglomerative Clustering as implemented by the
191 SciPy library on the Hough-transformed datasets (Müllner, 2011; Virtanen et al., 2020)(Fig-
192 ure 1c). Agglomerative clustering is a bottom-up hierarchical clustering method that re-
193 cursively pairs samples together with the closest nearby cluster until a set distance thresh-
194 old is reached, after which clusters will not be merged.

195 We chose Agglomerative Hierarchical Clustering (AHC) due to the multiscale struc-
196 ture of the dike swarms and the observational dataset. On the dike scale level, field ob-
197 servations can include multiple segments of a dike structure oriented in the same direc-
198 tion. These segments have been unlinked due to exposure bias or small changes in sur-
199 face expression such as en echelon segments. The dike scale is limited to the width of
200 a single dike packet in the system. The other scale is the mesoscale structure of the dike
201 swarm. This represents the packets of dikes aligned due to magmatic or tectonic stress.
202 Analysis of the large scale dike swarm structure can provide information about these forces
203 change laterally/temporally. Given the hierarchical nature of clustering, the AHC algo-
204 rithm allows data analysis on the two (or more scales) in a natural manner.

205 The AHC algorithm requires the choice of two parameters for unsupervised clus-
206 tering. First, the linkage method which determines how the proximity between two ob-
207 jects in a cluster is calculated. We choose complete linkage in which the proximity of two
208 clusters is the distance between the two most distant objects (Sorenson, 1948). This link-
209 age scheme yields more “compact” clusters and maintains strict criteria for dike segment
210 linking (Everitt, 1980). Another common linkage scheme is the single linkage, in which
211 proximity is the minimum distance between two objects in a cluster. However, a chal-
212 lenge with this linkage is that can lead to “chaining” of events and consequently form
213 stringy clusters. Complete linkage doesn’t suffer from this drawback and also has the ad-
214 vantage of allowing us to set a maximum distance for all clusters. So by definition, no
215 object in a cluster will have distances greater than a prescribed parameter which is not

216 the case in single or average linkage (Everitt, 1980; SNEATH, 1957). Despite potential
 217 concerns about the sensitivity of the results to the linkage choice, we find that average
 218 and complete linkages only had a minor impact on number of linked dikes, median lengths,
 219 and widths. This is because for most clusters only two samples are included in each cluster.
 220 In contrast, using single linkage would cause event chaining for the datasets, which
 221 we deemed undesirable for our research question. For each data set, the optimal choice
 222 of linkage parameters can vary based on the demands of the research problem.

223 The second parameter is the distance over which the clusters will not be merged
 224 (d). We find that this is the most critical algorithmic parameter. The goal of our clustering
 225 analysis is to link segments that may be on the same line or along a narrow axis.
 226 Thus, we use a Euclidean distance metric to determine the distance between data in the
 227 HS scaling it by the angle cutoff ($\delta\theta$) and intercept cutoff ($\delta\rho$):

$$228 \quad d = \sqrt{\left(\frac{\theta_1 - \theta_2}{\delta\theta}\right)^2 + \left(\frac{\rho_1 - \rho_2}{\delta\rho}\right)^2} \quad (4)$$

229 For each dataset, we choose strict angle cutoffs of 2° while setting the intercept cutoff
 230 to the mean length of the dike segments. We choose this limit because it is representative
 231 of the smaller segment-scale length in the databases. Our Sensitivity analysis for
 232 the CJDS dataset suggests that changing the ρ cut off has minor impact on the results.
 233 In contrast, changing the angle cutoffs can unsurprisingly affect the results a fair bit.

234 We set the distance cutoff (d) in the AHC algorithm to 1. This implies that if two
 235 points are exactly parallel ($\theta_1 = \theta_2$), their distances must be less than or equal to $\delta\rho$
 236 from each other in order to cluster together. A schematic illustration of the AHC and
 237 dike linkage process is shown in Figure 1.

238 ***2.2.1 Robustness and Dike Characteristics***

239 After linking is performed on the Hough Space, we examine the clusters in both
 240 Hough and Cartesian coordinates for robustness. There are two ways in which transform-
 241 ing between Hough Space and Cartesian space can introduce distortion. First, the dif-
 242 ference between two values of the line ρ is approximately equal to the perpendicular dis-
 243 tance between two parallel lines. However, there is distortion of this value far from the
 244 coordinate origin. In the Supplement, we show that this occurs increasingly for large dif-
 245 ferences in angle but can be avoided by comparing only segments with similar θ . Far from
 246 the Hough origin dikes are less likely to be clustered together due to distortion between

247 the Hough space and Cartesian space. Overall, distortion in the data would prevent dikes
 248 that are similar from being clustered but it will not create false clusters. We combat this
 249 by choosing a coordinate origin which is the mean of segment midpoints and by break-
 250 ing up the large data sets into subswarms.

251 Second, in Hough space, lines with -90° and 90° have the same horizontal orien-
 252 tation (E-W from a map point of view). To solve this issue in Hough space clustering
 253 we simply rotate the dataset so that the median angle is centered on 20 degrees. This
 254 minimizes the number of clusters that would need to cross -90° and 90° and 0° .

255 Finally, in the Hough space, lines are assumed to be infinite so the clustering does
 256 not account for where a segment falls on the line. We calculate a variety of metrics to
 257 give a sense of how the segments in a cluster are oriented to give a sense of structure.
 258 In Cartesian space, to find a new line segment to represent the cluster, we take the av-
 259 erage orientation from all segments and extend the line so that its tips represent the ex-
 260 tremity of the individual segment endpoints.

261 We fit a rectangular box around the group of segments to find the dike segment
 262 ‘packet’ length and the dike segment ‘packet’ width, where the length is oriented along
 263 the packet orientation and the width is measured perpendicular to the length. ***When***
 264 ***referring to cluster length or width, we are referring to this measure and not***
 265 ***individual segments.*** As another measure of cluster distribution in Cartesian space,
 266 we calculate the maximum Euclidean nearest-neighbor distances between segment mid-
 267 points. This value is then normalized by the length of the cluster. For a cluster of only
 268 two segments, this number is always 1. For larger clusters, this number represents the
 269 distance between the two furthest segments. We assume that clusters where the two fur-
 270 thest segments are significantly far from each other, over half the length of the cluster,
 271 are less robust. **In subsequent analysis, we will refer to the subset of clusters**
 272 **filtered first by cluster size (> 3 segments) and by the maximum nearest-**
 273 **neighbors distance (< 0.5) as the ‘filtered’ database.**

274 2.3 Datasets

275 In this study, we have chosen three datasets to focus on and apply our methods.
 276 First, the Spanish Peaks which represents a edifice scale structure. Second, the Columbia
 277 River Basalt Group data set which includes four subswarms (Ice Harbor, Chief Joseph,

278 Monument, and Steens) with the majority of our attention paid to the largest, the CJDS.
279 Finally, we apply our method to the CFB province scale and examine the Deccan Traps
280 datasets and the major subswarms (Central, Coastal, Narmada-Tapi, and Saurashtra)
281 (GSI District Resource Map, 2001; Mittal et al., 2021; GSI Bhukosh, 2020 (accessed De-
282 cember 1, 2020)). The Spanish Peaks dataset acts mainly as a test dataset for our meth-
283 ods while we will compare the two CFB related swarms to investigate qualitatively the
284 characteristics of CFB dikes. For each of the CFB datasets, the clustering is performed
285 on the subswarm level to minimize Hough Transform (HT) distortion from the choice
286 of an origin (refer to Table 1 for specific clustering parameters).

287 All datasets go through a preprocessing step to eliminate dikes that have non-linear
288 shapes. Each dike in a ESRI shapefile is read as a set of points and is then fit to a line
289 using the SciPy linear regression library (Virtanen et al., 2020). Dikes with a non-significant
290 p-value $p > 0.05$ are excluded from the linking dataset. The line fit is then used as the
291 line for the linking algorithm. Based on the unique start and endpoints of each dike seg-
292 ment, each dike is given a unique ID so that they are identifiable even after coordinate
293 transformations. Clusters are given cluster IDs based on the hash of the list of segments
294 in each cluster. Each dike segment data set is formed as a Python Pandas DataFrame
295 for ease of use and readability while it is used within the algorithm and for analysis (McKinney
296 et al., 2011; pandas development team, 2020). Data is then output as a CSV spreadsheet
297 and end points of the linked dikes are written as Well Known Text (WKT) vector ge-
298 ometry objects which is then readable in GIS software.

299 ***2.3.1 The Spanish Peaks dike swarm***

300 The Spanish Peaks area is located in southern Colorado in the Rio Grande Rift and
301 is made up of two intrusive stocks and associated dikes in Tertiary sediments (Figure 2e,f).
302 Spanish Peaks is one of the most commonly cited and studied radial dike swarm (Johnson,
303 1961; Odé, 1957). Each intrusive body and the associated dikes represent distinct mag-
304 matic phases and compositions (Penn & Lindsey, 2009). The nearby Dikes Mountain or
305 Silver Mountain lies 50 km NW of the Spanish Peaks, and its associated dikes are syen-
306 odiorite (Johnson, 1961). Although the exact relationship between the two stocks and
307 Dike Mountain is unclear, the Dike Mountain is dated as older than the Spanish Peaks
308 intrusions (Penn & Lindsey, 2009). We chose to include these dikes in our database to
309 demonstrate the algorithm's ability to differentiate between two closely oriented radial

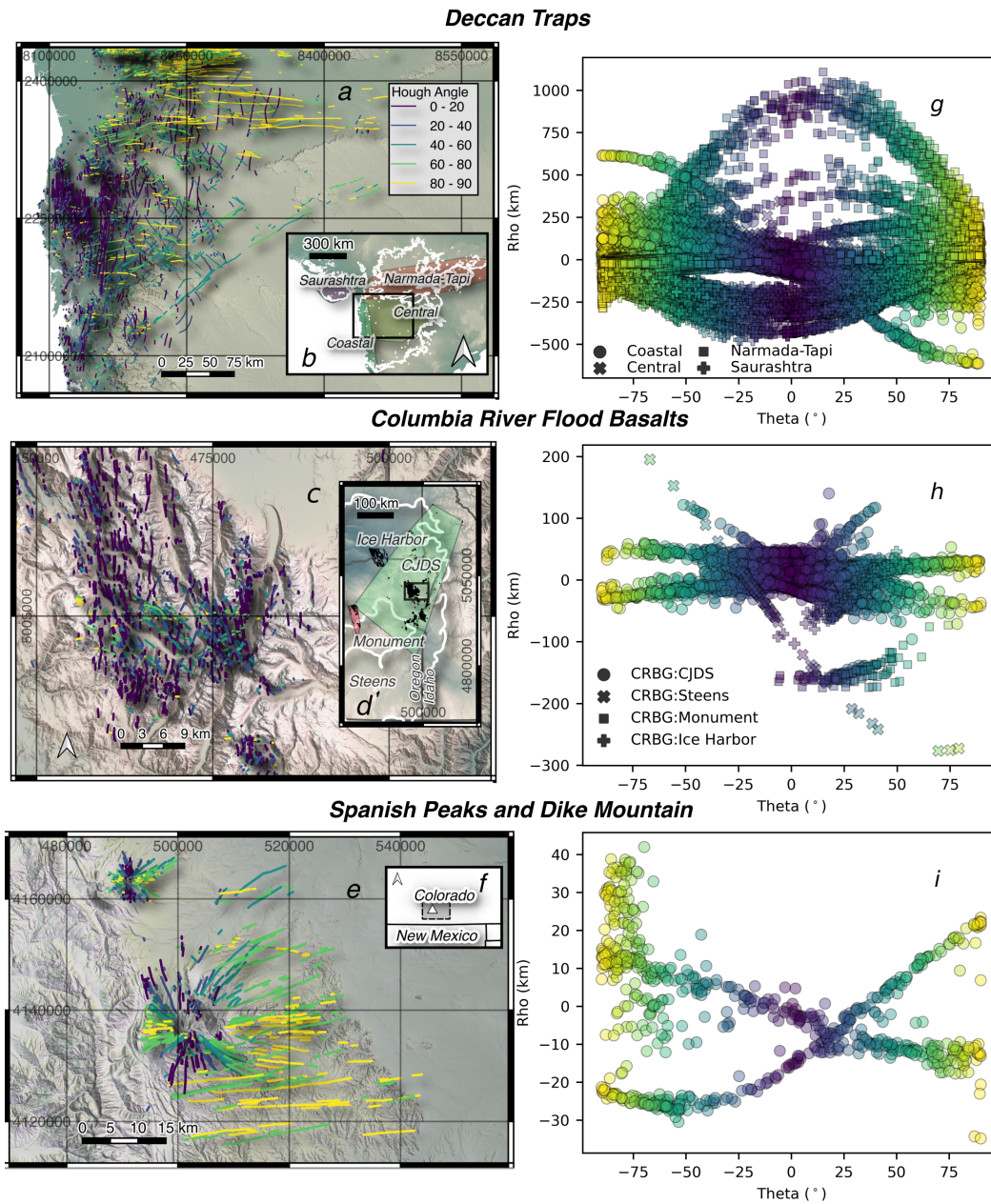


Figure 2. Map figures showing portions of the three datasets (**A.**, **C.**, **E.**) with the large scale structure show in the insets (**B.**, **D.**, **F.**) along with their respective structure in the Hough Transform space (**G.**, **H.**, **I.**). All figures show the absolute value of the dike segment angle (θ) colored in terms of the colorbar in **A.**

310 swarms. Using this full dataset, we can also test our method’s ability to devolve spatially
311 overlapping radial and linear swarms. The dikes were digitized based on mapping in Johnson
312 (1961) producing a shapefile of all dikes (linear and curving). These dike segments are
313 then preprocessed using the steps described earlier. The final database used for cluster-
314 ing is available in the supplemental material of this publication as CSV with WKT.

315 ***2.3.2 Columbia River Basalt Group Dataset***

316 From the CRBG, we investigate the Chief Joseph, Ice Harbor, Steens Mountain,
317 and Monument dike swarms both individually and together as compiled in Morriss
318 et al. (2020) (Figure 2a,b). The CRBG is the youngest flood basalt province on Earth
319 and covers an area of approximately 210,00 km² (Reidel, Camp, Tolan, Kauffman, &
320 Garwood, 2013). Like other CFBs a majority of the CRBG was erupted in a short ‘main
321 phase’ pulse, 17.2 Ma to 15.9 Ma with narrowing windows in progressive studies (Reidel,
322 Camp, Tolan, Kauffman, & Garwood, 2013; Kasbohm & Schoene, 2018). Previously, dike
323 swarms associated with CRBG have been linked together to form a radial dike swarm
324 originating from an extensive centralized magma chamber in eastern Oregon (e.g. Glen
325 & Ponce, 2002; V. E. Camp & Ross, 2004; Wolff et al., 2008).

326 The Ice Harbor subswarm is associated with post-main phase Saddle Mountain Ice
327 Harbor flows dated at 8.5 Ma (Reidel, Camp, Tolan, & Martin, 2013). The dike posi-
328 tions are inferred by high-resolution aeromagnetic survey (Blakely et al., 2014; Morriss
329 et al., 2020). The dikes appear mostly linear and strike N-NW at approximately $27 \pm$
330 11° . Monument dike swarm (Fruchter & Baldwin, 1975; Cahoon et al., 2020) located in
331 central Oregon was mapped to have a similar orientation to the Ice Harbor swarm $30 \pm$
332 14° . Our Steens dike database consists of 69 basaltic dikes exposed on the flanks of Steens
333 Mountain mapped by satellite imagery in Morriss et al. (2020). Steens dikes show a range
334 of orientations and represent both the most southern exposures of dikes in the database.
335 These dikes likely are linked to the CRBG’s earliest eruption of the Steens Basalt (Kasbohm
336 & Schoene, 2018; Morriss et al., 2020).

337 The largest of the CRBG associated databases, the Chief Joseph Dikes Swarm (CJDS)
338 is mainly located in the Wallowa mountain regions of Eastern Oregon covering an area
339 100 km wide by 350 km long. The CJDS has been linked via geochemistry to the main
340 phase formations of the CRBG : the Imnaha and Grande Ronde basalts. However, geo-

341 chemistry has revealed compositions spanning nearly the entire range of CRBG erup-
342 tion members (H. L. Petcovic & Dufek, 2005; Morriss et al., 2020). This suggests the area
343 was a hub of overlapping intrusive activity for significant periods of time. This is also
344 supported by the high segment density throughout the region of up to 5 segments/km².
345 Overall, CJDS exhibits a linear orientation with strike NW at $6.0\pm 30^\circ$. However, sig-
346 nificant secondary trends offset in angle is also present for the dike swarm which com-
347 plicates the view of the swarm as singularly linear.

348 ***2.3.3 Deccan Traps Dataset***

349 The Deccan Traps flood basalt consist of four main dike swarms the Saurashtra swarm,
350 Narmada-Tapi, which extends from Saurashtra through the Mandla Lobe, the Coastal
351 Western Ghats swarm, and east of that the Central Dike swarm or Nasik-Pune swarm
352 (Mittal et al., 2021) (Figure 2c,d). The dike dataset was compiled by Mittal et al. (2021)
353 resulting in 29,000 dike segments based on a variety of sources including satellite imagery,
354 district resource mapping, and digital elevation maps but the majority of segments are
355 based from Geological Society of India field mapping (1:50k maps, (GSI District Resource
356 Map, 2001; GSI Bhukosh, 2020 (accessed December 1, 2020))).

357 The western Narmada-Tapi region shows the highest density of dike segments and
358 appears largely linear with ENE-WSW orientation along the rift-graben structure (Ray
359 et al., 2007; Shukla et al., 2022). Dike segments decrease in frequency from west to east
360 but are often clustered around rift-faults (Bhattacharji et al., 1996). The Saurashtra sub-
361 swarm shares strong ENE-WSW orientation but also exhibits a range of angles. The Coastal
362 Swarm, located along the Western Indian coast, shows a N-S orientation along the West-
363 ern Ghats escarpment (Vanderkluyzen et al., 2011; Self et al., 2022a). Finally, the Cen-
364 tral or Nasik-Pune swarm shows little angle preference and has some of the longest in-
365 dividual segments lengths (up to 69 km, (Mittal et al., 2021)). In previous studies, the
366 Central and Coastal swarms have been roughly separated by the Western Ghats escarp-
367 ment. However, we choose to combine these two swarms due their large overlap in Hough
368 Transform space and the presence of mapped dikes that cross this boundary (See Fig-
369 ure 2c,d). We will refer to it collectively as the "Deccan Central swarm" in the rest of
370 the paper.

[ht]

Table 1. Hough transform and clustering parameters for each dataset

Dataset	Dike Segments No.	Rho Threshold (m)	HT Center Location (UTM)	Cluster No. (Total/Filtered)
<i>Spanish Peaks</i>	698	2013	(-11684090, 4503618)	191/28
<i>CRBG:CJDS</i>	4064	433	(475083, 4976408)	1057/91
<i>CRBG:Monument</i>	103	1201	(306813, 4943505)	20/1
<i>CRBG:Ice Harbor</i>	112	4410	(369188, 5104698)	31/1
<i>CRBG:Steens</i>	61	408	(370992, 4721712)	10/1
<i>Deccan:Central</i>	5512	3436	(8174542, 2237149)	1459/219
<i>Deccan:Narmada-Tapi</i>	11788	1730	(8403558, 2495692)	2279/600
<i>Deccan:Saurashtra</i>	8638	1562	(7907507, 2440048)	2108/405

371 We anticipate that both the CFB datasets are likely incomplete due a combina-
 372 tion of vegetation cover, lack of exposure, and the large areal extent. Thus, they are ex-
 373 cellent candidates for our clustering algorithm to link individual dike segments (Mittal
 374 et al., 2021; Morriss et al., 2020). In both cases, the majority of outcrops occur at shal-
 375 low paleodepths. The paleodepth of the CJDS is estimated to be ≈ 2 km (Morriss et
 376 al., 2020). The depth of original intrusions for Deccan is unknown but is also likely shal-
 377 low since a large majority of the dikes are emplaced in either Deccan basalt or shallow
 378 basement (Ray et al., 2007; H. C. Sheth & Cañón-Tapia, 2015; Shukla et al., 2022). Many
 379 other giant dike swarms have also been shown to have relatively shallow to mid crustal
 380 depths of 6–15km (Ernst et al., 1995). The limited vertical exposure limits the infer-
 381 ences about the deep crustal plumbing systems in CFBs. Nevertheless, the dike swarms
 382 are extremely important for understanding how magma is erupted from CFBs and thus
 383 what effects such voluminous eruptions would have on the atmosphere and biosphere.

384 **3 Results - Dike Lengths and Widths**

385 We applied the Hough Transform to dike segment databases from the Spanish Peaks,
 386 Deccan Traps, and CRBG then performed clustering in the Hough space to link clus-
 387 ters with similar orientations. For each dataset, we have a filtered database of clusters
 388 which is significantly longer than the original segment database.

389 In Figure 2g,h,i, we show the corresponding data from the Hough Transform seg-
 390 ment data for each of three datasets. Applying our dike linking algorithm to this, we find
 391 that we can successfully reproduce the dike swarm structure for Spanish Peaks. As an
 392 example of what the algorithm does visually, we show three representative examples of
 393 three clusters from the Chief Joseph, Deccan Central, and Deccan Narmada-Tapi dike
 394 swarms respectively (Figure 3)

395 On a full dataset scale, we see significant increases, by up to three orders of mag-
 396 nitude, in dike cluster length compared to the segment database (Figure 4). This is seen
 397 for all three datasets and also at the subswarm scale. Furthermore, the filtered dike dataset
 398 (clusters with size > 3 and max nearest neighbors distance < 0.5) are on average longer
 399 than the full clustered database. We do not account/incorporate clustered dike length
 400 in the filtering step and find that there is only a weak positive relationship of cluster size
 401 and cluster length (See Figure S3). We find that very long dike clusters (> 200 km) have

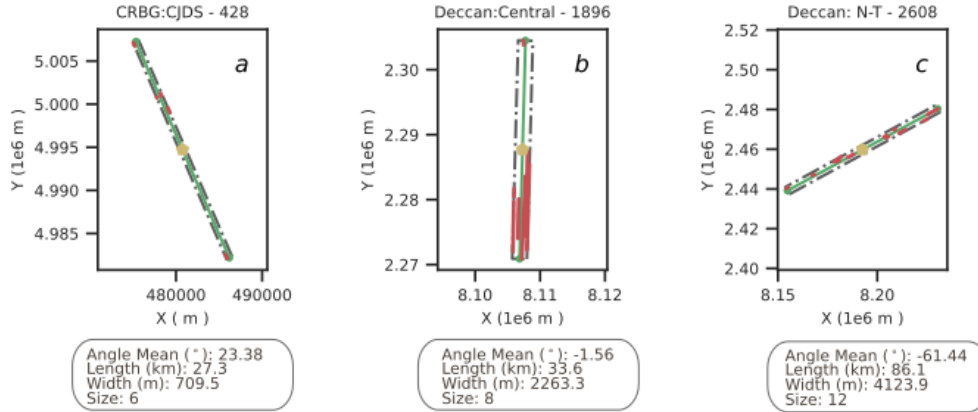


Figure 3. Example clusters from the Chief Joseph, Deccan Central, and Deccan Narmada-Tapi dike swarms (a,b,c respectively). The red lines show the mapped dike segments, the dashed grey box shows a rectangle fitted around segments while the green line shows the average line of the cluster.

402 cluster sizes of 2-18 although clusters of over 5 are relatively rare. Overall, the results
 403 of our dike linkage analysis for the three datasets strongly suggests that dike swarms mapped
 404 as distributions of many disconnected segments actually represent a smaller set of struc-
 405 turally continuous structures.

406 The Deccan Traps dikes show the longest dike clusters with the extrema reaching
 407 over 1000 km and a median length of 55 km. Although the individual segment lengths
 408 are roughly similar between the Saurashtra and Narmada-Tapi subswarms, the Narmada-
 409 Tapi swarm shows the longest linked dikes of all subswarms, eclipsing even the longer
 410 segments of the Central swarm.

411 The utility of our linkage algorithm is even more clearly exemplified for the CRBG
 412 dataset. Before clustering, this dataset had the short segments with an average length
 413 of only 400 m. However, after linking, the dike clusters have a median length of 10.6 km
 414 with some dikes reaching over 200 km. Within the CRBG dataset, the Ice Harbor and
 415 CJDS show the longest lengths but we note that these segments are inferred through aero-
 416 magnetic survey (Blakely et al., 2014) as opposed to field survey for CJDS dataset.

417 The second scale over which we can evaluate diking activity is dike or cluster width.
 418 The median dike segment width observed in the CJDS dataset is 8 m. It is slightly higher
 419 for the Deccan dikes at 10 m, although the available segment width data on Deccan dikes

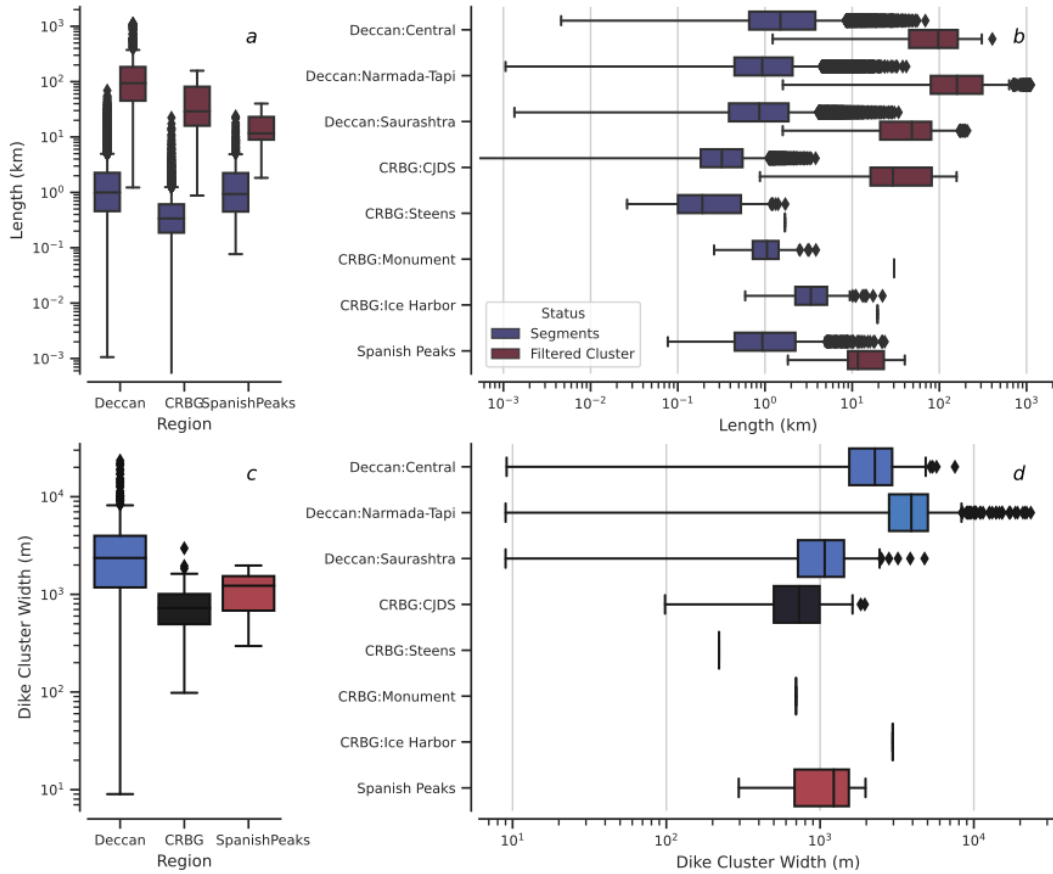


Figure 4. **A.** Log-scale lengths of the segment database and filtered linked database in blue and red, respectively for the three regional databases. **B.** Lengths broken down by subswarm for each region. **C.** Log-scale widths of dike clusters found in the linked database, and filtered linked database in blue and red respectively for the three regional databases. **D.** Dike cluster widths are shown broken down by subswarm for each region.

420 is relatively sparse (Ray et al., 2007). After clustering, the Deccan shows higher dike packet
 421 widths (~ 2300 m) than the CRBG (~ 700 m) or Spanish Peaks (~ 1200 m). This is
 422 not surprising given the higher ρ clustering thresholds (See Section 2.2) for Deccan. In-
 423 terestingly, the dike “width” is also the largest for the Narmada-Tapi swarm (~ 3 km)
 424 compared to ~ 2 km and ~ 1 km for the Central Deccan and the Saurashtra swarms re-
 425 spectively. This suggests that the longest Narmada-Tapi linked dikes are composed of
 426 a number of commonly oriented linear features.

4 Discussion

We examine the LIP cluster databases in both Cartesian and Hough spaces to evaluate the dike swarm structure over a variety of scales. We start by looking at the scale of individual dikes (10s km) and move onto the large scale (> 100 s kms) then finish with discussion of mesoscale structures (linear and radial type swarms on the scale of 10s-100s km).

4.1 What do the dike clusters represent?

4.1.1 Linear Elastic Mechanics analysis

Dikes are classically modeled as isolated fluid-fluid opening mode (Mode I) fractures (Rubin, 1995). Dike widths and lengths are related to each other based on the magma overpressure and host rock properties (Rubin, 1995; Gudmundsson, 2002). Using LEFM, the predicted scaling for the length to width ratio is

$$\frac{L}{W} = \frac{E}{2\Delta P(1 - \nu^2)} \quad (5)$$

where L is the length, W is the width, E is the Young's Modulus, ν is the host rock Poisson's ratio, and ΔP is the magmatic over pressure. Using typical values, $E = 10 - 30$ GPa, $\nu = 0.25$, and $P = 1 - 10$ MPa), we expect this ratio to be $\sim 10^3 - 10^4$.

In Figure 5a we have plotted the dike cluster width and dike cluster length with three scaling ratio lines plotted over them (10^3 , 10^1 , 10^1). The CJDS data shows a bimodal distribution with one peak falling on the 10^2 line and the other falling between the 10^2 and 10^1 lines. The Deccan dikes are overall wider and longer than the CJDS dikes and fall mostly between the 10^2 and 10^1 lines but with a significant portion on or above the 10^2 ratio line. Breaking down the Deccan subswarms we find that Saurashtra subswarm shows overall shorter dike cluster lengths and widths more in line with the CJDS while the Deccan Central and Narmada-Tapi subswarms show significantly longer dikes. Overall, few clusters are close to the 10^3 ratio. Thus, we conclude that our dike clusters do not follow the expected LEFM predictions and are typically too wide. One potential explanation for our results is that the effective crustal strength on large scales is weaker than the rock material properties due to presence of pre-existing fractures, thermal stresses from dike emplacement, and/or some viscoelastic stress relaxation (J. Kavanagh & Pavier, 2014; Eberhardt, 2012; Ma et al., 2020; Thiele et al., 2020).

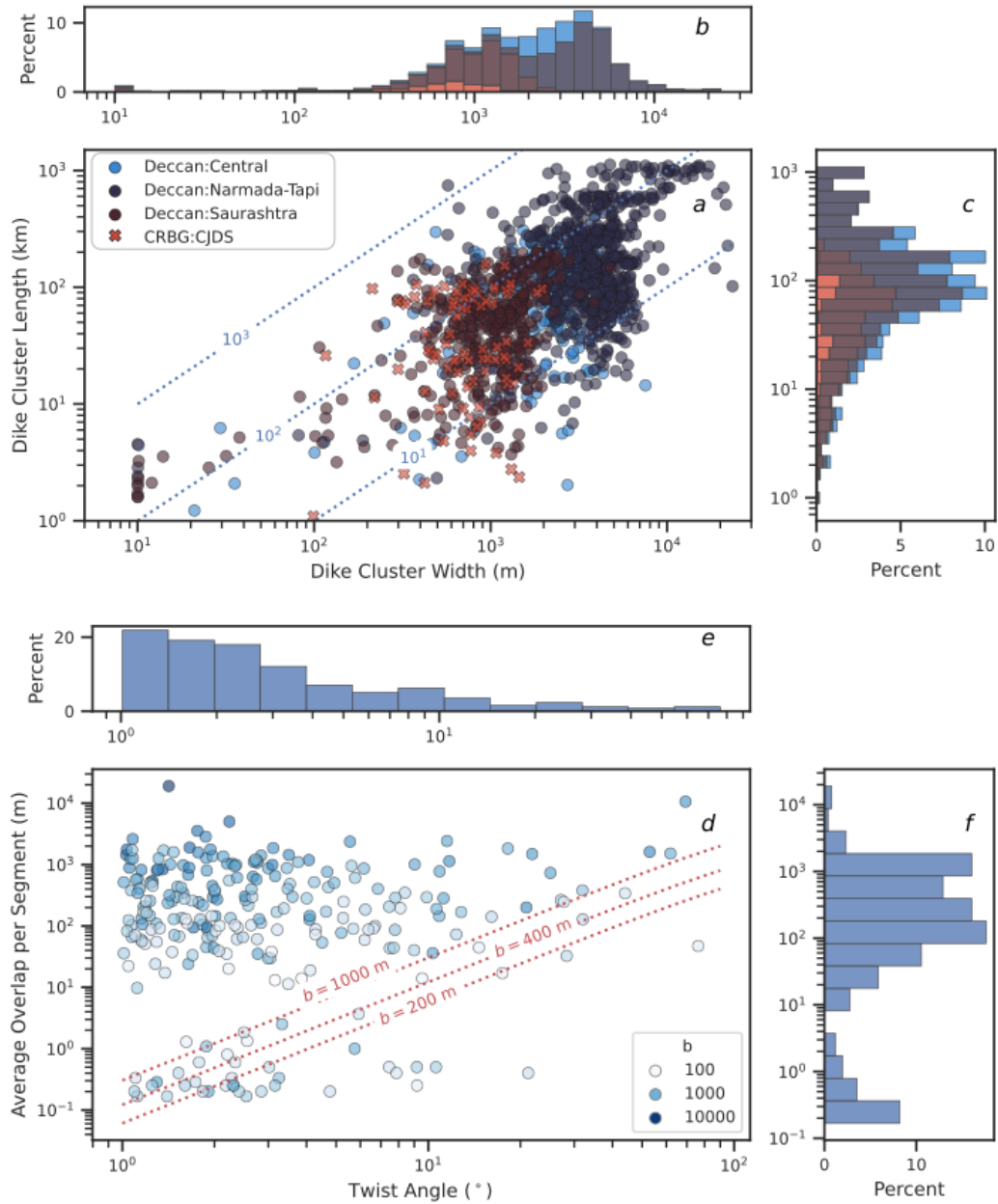


Figure 5. **A.** Log-scale widths of dike clusters plotted against the log-scale dike cluster lengths. Three trend lines (blue dashed lines) are plotted over the data showing length to width ratios of 10^3 , 10^2 , 10^1 with the majority of the data plotting between the 10^3 and 10^2 trend-lines. Despite these different values, the median aspect ratios are similar 53 vs 48 for the Deccan and CRBG. **B.** and **C** show the distribution of the dike cluster widths and lengths respectively. **D.** plots the twist angle in degrees versus the calculated average overlap per segment in meters (log-scale) only for a subset of the data ($n = 256$) which has twist angle of over 1° and overlap of over 0.1 m. The color of the dots indicates the half-segment length (b). In red dashed lines, three trend lines are plotted over the data indicating b values of 200 m, 400 m, 1000 m, which are representative of average values seen in the different datasets. **E.** and **F** show the distribution of twist angle and overlap respectively.

457 To further evaluate intra-cluster distribution of segments, we examine predicted
 458 scaling for isolated dikes in a spatially variable (rotated) stress field, which often exhibit
 459 segmented or ‘en echelon’ distribution (Pollard et al., 1982). To do this we look at the
 460 overlap between segments and the twist angle (Figure 5). Twist angle is calculated as
 461 the difference between the mean angle of the cluster and the line of best fit over the cluster
 462 midpoints. A twist angle of zero indicates the segments are aligned with the other
 463 segment endpoints. A higher twist angle indicates that the segments are offset from the
 464 line of their midpoints which could indicate en echelon type fracturing.

465 En echelon type fractures mix Mode I and Mode II type fractures due to changes
 466 in the regional or local stress field due to material inhomogeneities (Rubin, 1995; Pol-
 467 lard et al., 1982). We calculate the total overlap across the cluster in meters then divide
 468 by the size of the cluster to find the average overlap per segment. Twist angle and over-
 469 lap can be related together for en echelon type fractures using the following equation:

$$470 \quad \mathcal{O} = b(1 - \cos(\omega)) \quad (6)$$

471 where \mathcal{O} is the overlap per segment, b is the segment half length, and ω is the twist an-
 472 gle based on equation 8b in Pollard et al. (1982) when the distance between segment mid-
 473 points is approximately equal to the segment half length. Due to the clustering param-
 474 eters, the distance between two segments is necessarily less than the segment average length.
 475 On Figure 5d, we show this calculation for various segment half lengths which span the
 476 representative values for the different datasets ($b = 200, 400, 1000$ m). Although some
 477 of the data is well represented by the lines, the majority of the data shows higher lev-
 478 els of overlap.

479 The spacing between dike segments in a cluster ($\delta\rho$) can also illuminate how the
 480 clusters were potentially formed. (Bunger et al., 2013) established a scaling analysis for
 481 the spacing of first generation fractures in a dike swarm and found it to be primarily de-
 482 pendent on dike height (H). They found that for a dike with time variable magma sup-
 483 ply, two potential scalings can arise : $\delta\rho/H \sim 0.3$ or $\delta\rho/H \sim 2.5$. Taking dike height
 484 to be approximately crustal thickness for LIP dikes ($H \sim 30$) and using the standard
 485 deviation of ρ in a cluster as the dike segment spacing, we find that our clusters do not
 486 follow the predicted ratio (~ 0.05 , still less than predicted even for $H \sim 10$ km). This
 487 suggests that dike segments are closer together than theoretical models. Notably the cut
 488 off for clustering based on ρ is also significantly less than the (Bunger et al., 2013) scal-

489 ing. Thus, our final conclusion isn't unexpected but it may support the idea that these
490 clusters represent multiple generations of dike.

491 **4.1.2 Summary Interpretation**

492 Based on all our analysis above, we posit that the clusters found using our algo-
493 rithm can present two possible interpretations: first, a cluster may represent a single frac-
494 ture that is one continuous magma pathway including a set of en echelon fractures which
495 have broken down due to rotations in the stress field; secondly, it may represent a fam-
496 ily of fractures which may have been emplaced over long periods of time. Figure 3 shows
497 examples of these different possible interpretations. Figure 3a shows short dike segments
498 aligned on a narrow area with high aspect ratio. Figure 3b however shows many segments
499 overlapping over a range of 2.2km and is unlikely to have been emplaced all at once. Mean-
500 while, Figure 3c shows a long cluster (86 km) with many segments oriented evenly across
501 its length with some overlap. However, this still may not represent a single fracture but
502 rather a series of related dikes are emplaced over time.

503 In conclusion, dike cluster length does not necessarily represent one uninterrupted
504 singular magma pathway or crack caused by fracturing (although in some clusters it may).
505 Instead, dike packet width is likely the zone of influence that a dike may exert in the shal-
506 low crust. Dike clusters are indicative of sustained areas of diking activity from crustal
507 magmatic system over a timescale when the regional stress field was relatively constant.
508 Looking at the overlap within a cluster (Figure 5d), we see more overlaps than would
509 occur in a simple en echelon fracture which may indicate that the observed overlaps are
510 due to emplacement of multiple dikes in a zone of weakness over time by reactivation.
511 Further, the continued magmatic emplacement in a localized region would reduce the
512 crustal strength and introduce local stress heterogeneity that can further change the dike
513 characteristics from the pure LEFM theoretical end-member. Notably, we are looking
514 only at the end state of the magmatic plumbing system so the dike scale is integrated
515 over the time of the activity.

516 Interpreting each cluster one-by-one is beyond the scope of this paper and would
517 require other information about the dike segments such as geochemistry, dating, and more
518 detailed field observations. Any additional data could be added to the clustering algo-
519 rithm for a higher dimension of clustering. However, our analysis suggests that clusters

generally represent multiple generations of dikes aligned along narrow axes of activity. The timescale of dike swarm emplacement is thus likely less than the timescale of changing regional stresses, or else the mechanical anisotropy induced by prior dike emplacement overwhelms the regional stress field. This interpretation of large CFB dike swarms provides supporting evidence for a trans-crustal, multi-magma reservoir magmatic architecture model for CFBs (Mittal & Richards, 2021). The spatio-temporal patterns in dike swarms may reflect an integrated lifecycle rather than a single time snapshot of the magmatic system (Black et al., 2021).

4.2 Large-scale Structure of Dike Swarms

At a province scale, dilation due to diking can cause significant strain in the upper crust and has implications for the emplacement of the plumbing system and the crustal stress field (Thiele et al., 2020). Dilation is calculated as

$$D(x_i) = \sum_{n=1}^N \bar{w} \cos(\theta) \quad (7)$$

for the EW direction and

$$D(y_i) = \sum_{n=1}^N \bar{w} \sin(\theta) \quad (8)$$

for the NS direction where x_i and y_i are bins in the EW and NS directions, N is the number of dikes in each bin, \bar{w} is the median width of the dike segment, and θ is the angle in Hough space. The average center of dilation is found by taking the weighted average of the bins using $D(x_i)$ and $D(y_i)$ as weights. These calculations can be performed for the segment or cluster database. The segment database provides a lower bound estimate of dilation while the linked clusters provide an upper bound, as long as our dike dataset is reasonably complete. We used a typical width of 8 and 10 m for the CRBG and Deccan respectively (Ray et al., 2007; Morriss et al., 2020; Shukla et al., 2022)

The CRBG is dominated by EW dilation as is expected by the dominantly NS trending CJDS. The maximum dilation seen in the segment database (~ 1300 m and ~ 1000 m for the EW and NS dilation respectively) are similar in magnitude but on average EW dilation is higher. For the clustered dataset however, maximum EW dilation significantly eclipses NS dilation (~ 3100 m and ~ 700 m for the EW and NS dilation respectively). The Deccan datasets show dominant NS dilation with ~ 2800 m and ~ 10800 m for the segment and linked databases respectively. The EW direction showed lower amounts of dilation with ~ 2500 m and ~ 4600 m for the segment and linked databases respec-

551 tively. This leads to a maximum strain of approximately 1% for both the Deccan and
552 CRBG datasets in their maximum directions of dilation and 0.3% and 0.14% in the min-
553 imum direction of dilation respectively. Notably, in both LIP datasets, the area-weighted
554 center of dilation implied by the clustered dike segments does not align with dike out-
555 crops.

556 **4.3 Identification of Mesoscale Spatial Structures in Dike Swarms**

557 A key motivating question for our work is whether LIP dikes are organized into co-
558 herent spatial patterns at a sub-swarm or swarm scale. Spatial structure of dike swarms
559 provides important constraints on dike-stress field interactions and external drivers of
560 dike emplacement. Magma chambers (Karlstrom et al., 2009; Gudmundsson, 2006), re-
561 gional tectonic stress (Wadge et al., 2016), and topography such as edifices (Roman &
562 Jaupart, 2014) have been inferred based on mesoscale patterns in the dike swarms. We
563 show that the Hough Transform can be a useful tool in evaluating a range of structures
564 in both the segment and linked databases, providing a means to overcome often incom-
565 plete and discontinuous observations.

566 **4.3.1 Synthetic Mesoscale Structures**

567 We will first focus on two end members of mesoscale dike swarm structure: linear
568 and radial (Figures 7A and B respectively). Roughly these two regimes represent either
569 a spatially consistent least principal stress axis, such as implied by tectonic extension
570 (Wadge et al., 2016), or a radially symmetric stress field such as implied by a magma
571 chamber, volcanic edifice, or mantle plume head (Ernst et al., 2001). These two end mem-
572 bers can coexist spatially if the stress field changes with time. Of the two, radial swarms
573 are more challenging to robustly identify in Cartesian space because apparent radial struc-
574 ture can arise from multiple misaligned linear swarms (Fig. 7C). These two end mem-
575 bers are more easily identified in the Hough space where a linear swarm is represented
576 by a vertical bar of points (Fig. 7a) and a radial swarm can be seen as a sinusoidal curve
577 spanning a sufficiently large range of angles. This is illustrated in Fig. 7b,c, with syn-
578 thetic line segment distributions. We also show some more complex swarm shapes and
579 the associated difference in Hough Transform space shapes (Fig. 7d,e,f). The synthet-
580 ics clearly illustrate that Hough Transform space is very useful to distinguish amongst

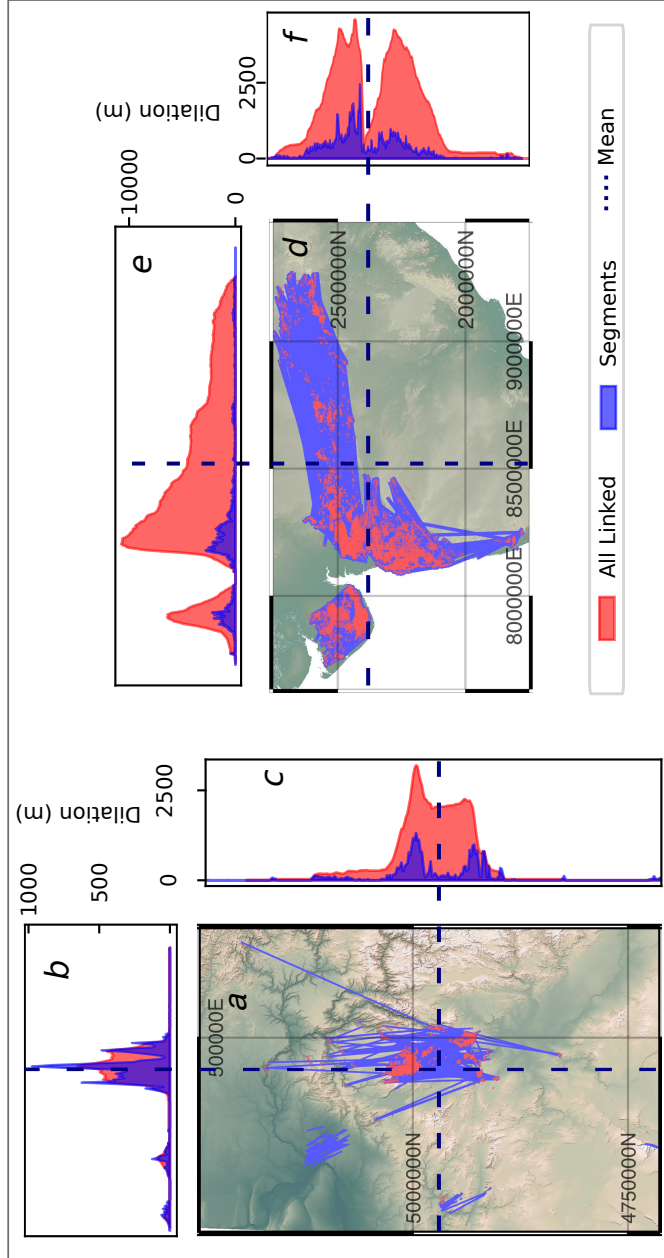


Figure 6. A. and D. show the segment database (red) overlaid on the linked clusters (blue) while the two side panels B. and C. and E. and F. show the dilation in the NS and EW directions for the segments and linked clusters of the CRBG and Deccan datasets respectively. The blue dashed line shows the segment density weighted center of dilation.

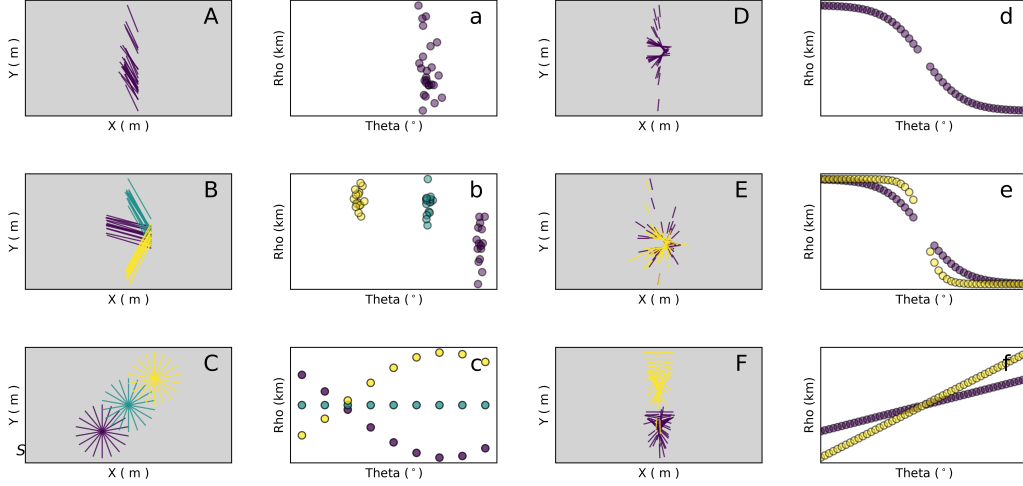


Figure 7. Synthetic dike swarms in a Cartesian space (gray background) and Hough Transform space (white background). **A.-C.** show relatively simple swarms while **D.-F.** show more complex shapes in Hough Transform space and their corresponding swarm in Cartesian space. **A.** and **a.** show a linear swarm centered around 30° . **B.** and **b.** show a radial swarm formed from three linear rays at 30° , 75° , -30° (green, purple, yellow). **C.** and **c.** show three overlapping radial swarms along a line. **D.** and **D.** show a sigmoid shape in Hough Transform space while **E.** and **e.** shows two overlapping sigmoids. **F.** and **f.** shows two straight lines in Hough Transform space with different slopes.

581 different kinds of dike mesoscale structure, although we focus only on end member pat-
 582 terns here.

583 We use several criteria to distinguish ideal radial dike patterns from other struc-
 584 tures. First, we assume that a radial dike distribution has a range of constituent angles.
 585 Secondly, we assume that the structure has a constrained area of intersection, interpret-
 586 ing this pattern as arising from a common magma source. To identify radial dikes, we
 587 return to the formulation of the Hough Transform in Eq. 1 and find an equation for a
 588 perfectly intersecting radial distribution of segments is

$$589 \quad \rho_r(\theta) = (x_r - x_c) \cos(\theta) + (y_r - y_c) \sin(\theta). \quad (9)$$

590 where x_r and y_r are the Cartesian location of the radial center adjusted by the chosen
 591 origin of the HT. Using Eq. 9 we can fit data in the Hough Transform space and find
 592 (x_r, y_r) a non-linear least squares to fit as implemented in Scipy Optimize library (Virtanen

593 et al., 2020). We can then pick any line which falls within $\rho_r(\theta) - R_{max} < \rho(\theta) < \rho_r(\theta) +$
 594 R_{max} which effectively draws a circle with radius R_{max} around the points (x_r, y_r) in carte-
 595 sian space and an envelope of half-width R_{max} around the line calculated in Eq. 9.

596 **4.3.2 Mesoscale Structures - Spanish Peaks**

597 To evaluate mesoscale structures in the Hough Transform space, we use the Span-
 598 ish Peaks dataset as a clear example of diverse structures. Spanish Peaks dikes exhibit
 599 three major components, first a radial structure centered on West Peak, a linear trend
 600 that strikes N. 60° E, and a secondary radial structure centered on Dike Mountain also
 601 known as Silver Mountain. The radial swarm of the Spanish Peaks is diffusely centered
 602 on West Peak although some dikes intercept outside the Peaks or in East Peak. West
 603 Peak is a quartz syenite dated to 24.6 ± 0.13 Ma while the East Peak is composed of
 604 granite and granodiorite porphyry dated to 23.9 ± 0.08 Ma (Penn & Lindsey, 2009). The
 605 dike compositions range from gabbro lamprophyre to granite porphyry (Johnson, 1961).
 606 The two radial structures and linear dikes overlap in Cartesian space but form distinct
 607 bands in Hough space (Figure 8).

608 We can apply the radial swarm equation to the Spanish Peaks dataset to find the
 609 center of the radial structures. First we segment the data using Northing value of the
 610 segment midpoint into two sections ($Y > 4520000m$ and $4480000m < Y < 4520000m$)
 611 then fit Eq. 9 with a radius (R_{max}) of 2.5 km (See Figure 8a,b). We find two radial cen-
 612 ters, one centered on West Peak (green, $R^2 = 0.75$) and another centered on Dike Moun-
 613 tain (purple, $R^2 = 0.93$). The distributions of angles in the radial swarm are mostly
 614 flat indicating even angular spacing except for slight increases around $-55^\circ - 90^\circ$ where
 615 some of the linear swarm dikes intersect with the radial swarm. For these specific dikes,
 616 it is ambiguous whether they should be counted as radial or linear. More data such as
 617 geochemistry could however differentiate them.

618 **4.3.3 Radial Swarms in LIP Datasets**

619 Applying the methodology described above to find radial structures in the larger
 620 LIP datasets, we first attempt to fit the entire datasets for CRB and DT respectively
 621 to Eq. 9 to find a common origin for the entire datasets. This provides a quantitative
 622 way to evaluate whether a single radial center fits the datasets, as has been suggested

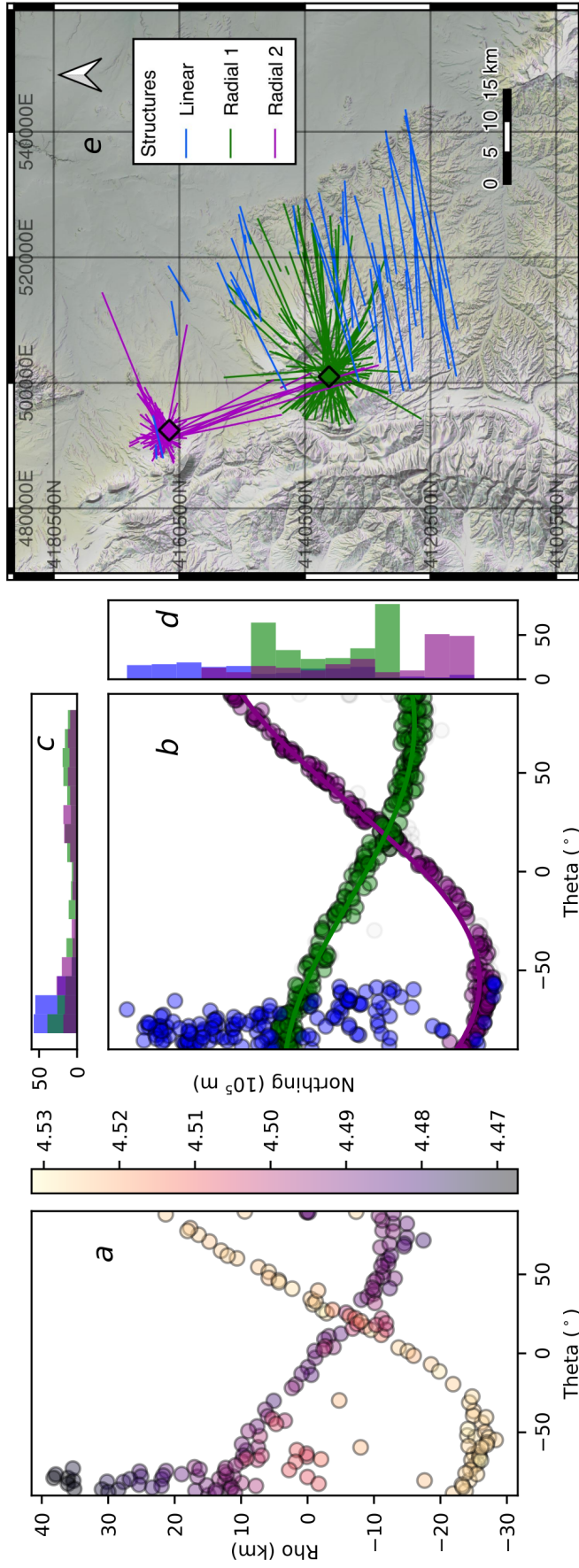


Figure 8. Analysis of the Spanish Peaks dataset. **A.** Hough Space colored by the segment midpoint Northing. **B.** Radial fits using Equation 9 and the segments which intersect within 2500 km of the centers and the remaining linear structure in blue. **C.** and **D.** show the distribution of θ and ρ respectively for the linear, and two radial structures. **E.** Clustered lines for the three identified structures in Cartesian coordinates.

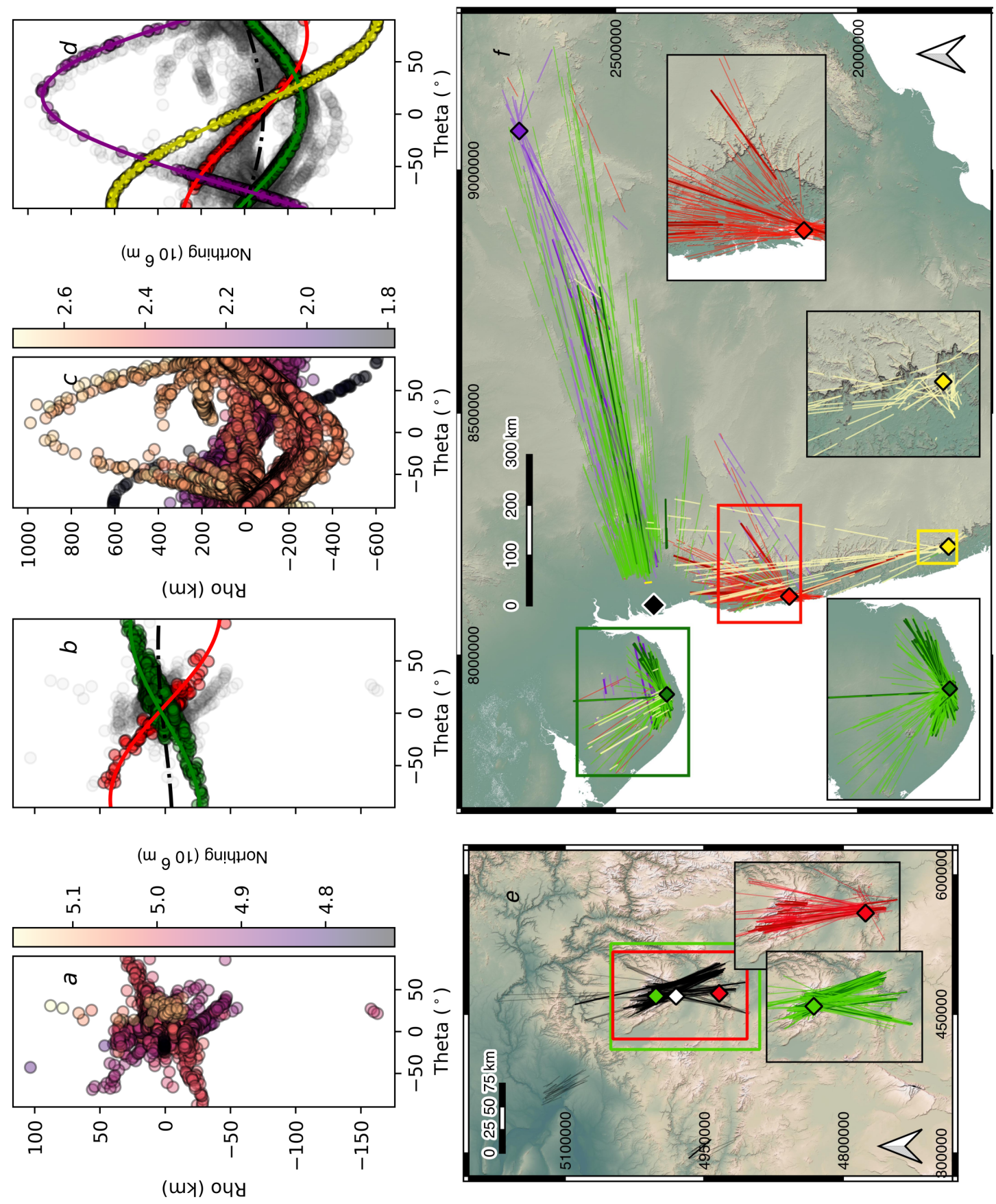


Figure 9. A. and C. show the Hough Space colored by the cluster midpoint Northing. B. and D. show possible radial fits using Equation 9. E. and F. show all clusters which fall within a 10 km radius of each radial center while the bold lines show the filtered lines which fall within this radius.

623 to result from impingement of an idealized radial plume head on the lithosphere (e.g. Ernst
 624 & Buchan, 1997). For both the CRBG and Deccan segment datasets (or linked datasets),
 625 we do not find a well fit radial center for the entirety of the dataset ($R^2 = 0.005$ and
 626 0.03 for CRBG and Deccan respectively, black diamonds). Thus, there is no evidence
 627 for a model wherein either an axisymmetric plume head or a large magma reservoir con-
 628 trols the dike pattern (See (Mittal et al., 2021) for discussion of various magmatic mod-
 629 els).

630 However, looking at subsets of the data sets, filtered based on segment midpoint
 631 Northing, we do find mesoscale radial patterns in both CFBs wherein all the dikes have
 632 intersections within a radius (R_{max}) of 10 km. In the CRBG datasets, we find two can-
 633 didate radial patterns – one centered in the Wallowa mountains region at (469438E, 5001913N
 634 - UTM Zone 11N, EPSG 26911 projection) and a second radial center south of the high-
 635 est density CJDS (472343E, 4933589N). The goodness of fit for these structures is how-
 636 ever low ($R_{sq} = 0.26, 0.15$ respectively) and the range of involved angles is not substan-
 637 tial. A more complex spatial pattern such a sigmoid shown in Figure 7B may provide
 638 a better fit to the dike segment distribution. We cannot rule out the possibility that ap-
 639 parent radial patterns in the CJDS simply arise from overlapping linear features with
 640 variable orientation.

641 In the Deccan database, we find several possible radial structures with significantly
 642 better goodness of fits than what is seen in the CRBG. Firstly, we find a center (Fig-
 643 ure 4.3.3, green) centered in the Saurashtra subswarm (7919544E, 2394058N - Pseudo-
 644 Mercator, EPSG 3857) with goodness of fit of $R_{sq} = 0.91$. Notably, this structure ex-
 645 tends well into the Narmada-Tapi rift zone which is strongly linear and is 100s of kilo-
 646 meters away. The fits do not account for Cartesian endpoints of the segments or clus-
 647 ters. The second best fit center is centered near Mumbai at 8121286E, 2141444N (Fig-
 648 ure 4.3.3, red) with goodness of fit of $R_{sq} = 0.81$. We show two other possible centers
 649 (Figure 4.3.3, purple and yellow) with high goodness of fit ($R_{sq} = 0.97$ and 0.99). How-
 650 ever due their large distance from the Hough Transform origin of the dataset, we are un-
 651 sure whether these swarms associations are physical (Figure 4.3.3f yellow inset). Upon
 652 closer analysis, we think that these linkages may be artifacts of Hough Transform dis-
 653 tortion (See Supplement for full analysis).

654 We believe that these apparent radial dike patterns in both CFBs warrant further
 655 study. In the CRBG, centralized magma storage south of the Wallowa mountains has
 656 been proposed (Wolff et al., 2008), which conceivably explains the southern-most radial
 657 center found via the Hough Transform and aligns roughly with the inferred centroid of
 658 dilation in Figure 4.2. However, the robustness of this structure is not very significant.
 659 For the Deccan Traps, the radial structures are more clear but no clear geological or geo-
 660 physical evidence of a localized magma reservoir associated with the center of the radial
 661 dike swarms has been recognized (Rajaram et al., 2017; Rao et al., 2022; Dole et al., 2022;
 662 Self et al., 2022b). Additional data is necessary to evaluate and assign physical interpre-
 663 tation to these structures.

664 *4.3.4 Linear Trends*

665 We consider a linear swarm to be defined by a set of subparallel dikes oriented along
 666 an axis. A linear swarm has a length and width in Cartesian space that correspond to
 667 a range of angles and ρ s in Hough Space. A narrow range in angles is essential. To iden-
 668 tify orientations with linear activity we examine the histogram of the Hough Space and
 669 look for concentrations of dikes within narrow bins of θ and ρ in a method analogous to
 670 the traditional use of the Hough Transform accumulator array (Figure 4.3.4). Looking
 671 at the bins with the highest counts, we can establish packets of linearly oriented dikes.
 672 The top three bins of the Hough Transform histogram for CRBG and Deccan represent
 673 11% and 12% of all segments respectively.

674 In the Deccan, the major linear trends are in the Narmada-Tapi rift zone between
 675 -85° and -65° and extend for well over 100 km and slightly into the Saurashtra region
 676 (Figure 4.3.4d). These overlap with the radial swarms found above and fall in the ra-
 677 dial swarm fits. The identification of dikes as being part of both a linear and radial struc-
 678 ture gives interesting information about the structure. This may be indicative of the fact
 679 that the presence of a slowly rotating stress field leads to the formation of multiple lin-
 680 ear type structures. These in turn overlap and forming a fanning radial swarm (similar
 681 to what is shown in Figure C). In CRBG, we find two subparallel axes of linear dikes struc-
 682 ture with high dike concentrations. These structures connect areas of high dike density
 683 which appear in the granites associated with the Wallowa mountains (H. Petcovic & Grun-
 684 der, 2003; Morriss et al., 2020).

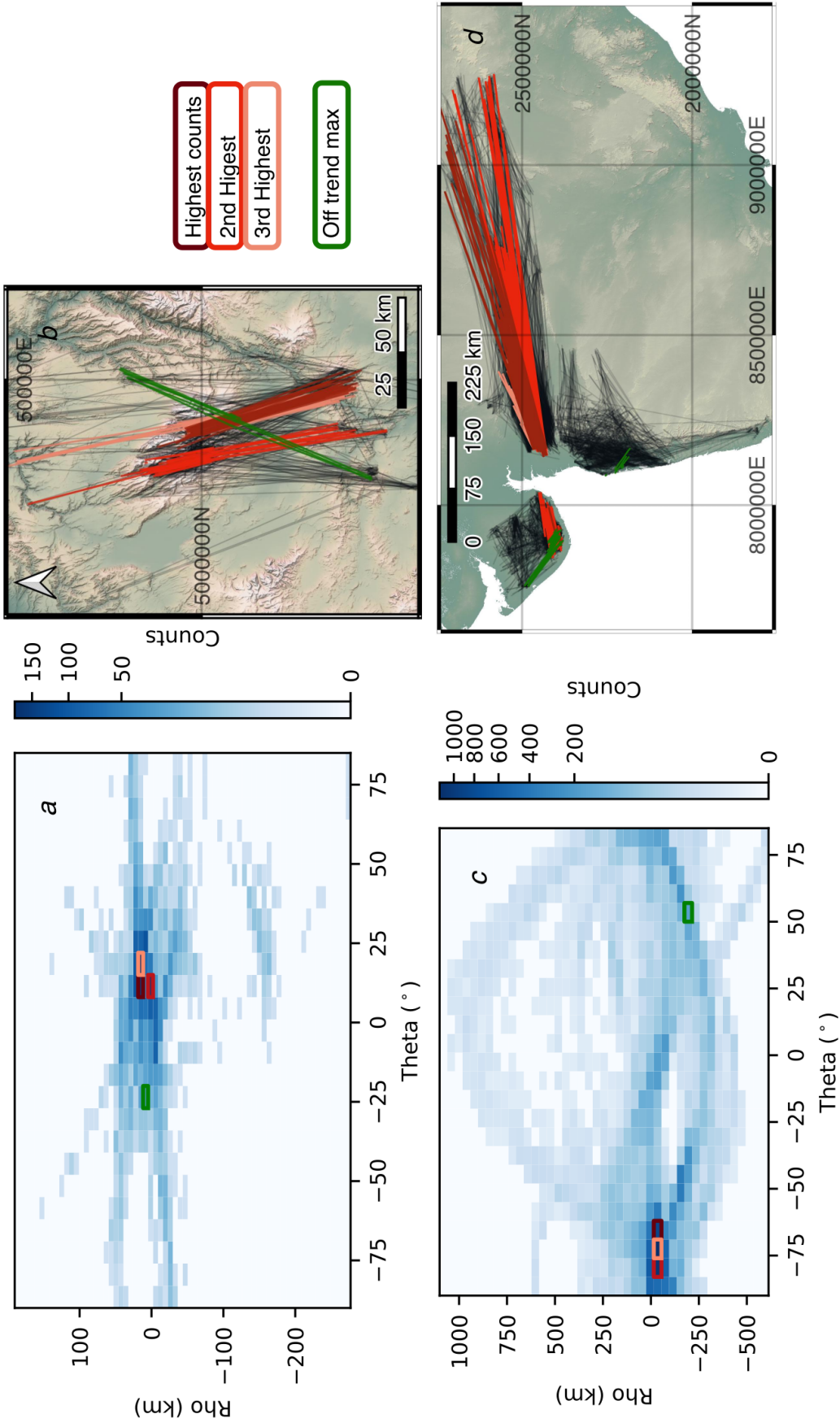


Figure 10. A. and C. show a histogram of the Hough transform segment database as a function of ρ and θ with dark blue colors indicating higher counts in that orientation. The bins of the histogram are set to be 7° in angle and 2.5% of the range of ρ . B. and D. show the top three bins of the histogram (maroon, red, and pink) in Cartesian space along with an off-axis maximum shown in green. The off axis maximum is the highest bin more than 50° away from the main linear trend (red box). We use the segment orientations for the histograms but show the linked dikes for ease of viewing.

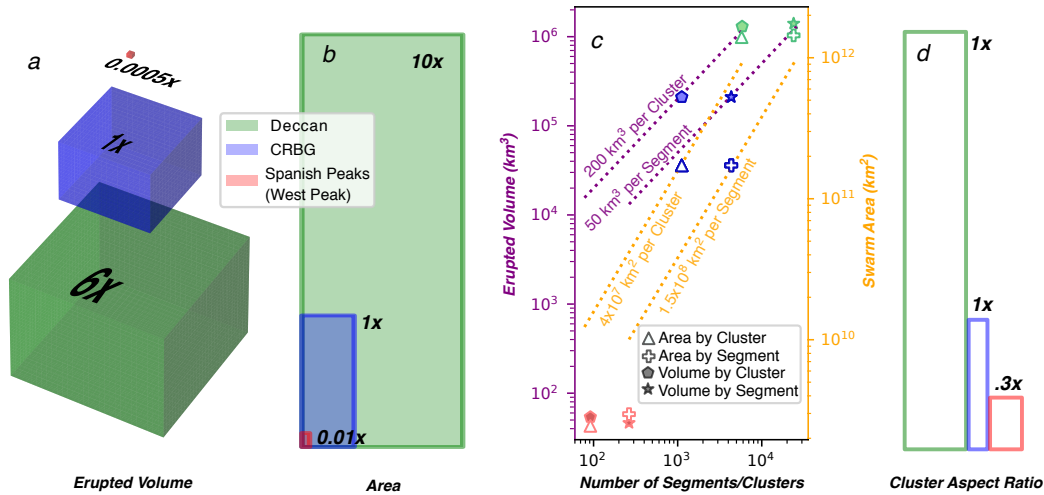


Figure 11. **A.** Comparison of the total erupted volume of Deccan Traps, CRBG, and Spanish Peaks (West Peak only). Due to lack of extrusive deposits associated with Spanish Peaks, West Peak erupted volume is estimated based on Grosse et al. (2009) assuming an intrusive:extrusive ratio of 1:2. **B.** Comparison of the swarm areas. **C.** plots the number of dikes or clusters versus the erupted volume (left, purple, filled symbols) and the swarm area (right, orange, white symbols) for the three dike swarms. Trend lines represent erupted volume and area per segment and cluster, roughly constant despite the limited data. **D.** shows the dike cluster aspects ratios are similar for the three examples.

4.3.5 Comparing Deccan and Columbia River Flood Basalts

685

686

687

688

689

690

691

692

693

694

695

696

697

The Deccan Traps erupted volume is at least 6x greater than the CRBG in eruptive volume (1,300,000km³ vs 210,000km³, Figure 4.3.5A) (Jay & Widdowson, 2008; Kasbohm & Schoene, 2018). Is this volumetric difference in erupted volume reflected in the shallow crustal dike swarm exposures? Most magma never erupts at the surface, so directly linking exposed dikes to eruptive volume in general is difficult (Townsend & Huber, 2020; Gudmundsson, 2002). Nevertheless, the large scale of upper crustal dike swarms as analyzed in this study provides a unique opportunity for comparison. Firstly, the Deccan dike segment database ($n = 25,938$) is larger than the CRBG ($n = 4340$) by a factor of 5.9, similar to the erupted volume ratio. Although there are significantly different observational biases, especially due to different exposure, in the CRBG and DT datasets we do posit that the difference in dike segment numbers reflects a more extensive crustal magma transport system for DT. In the unfiltered clustered database the

698 ratio (DT to CRBG) is also approximately maintained at $5.2x$. The filtered database
699 ratio is $13x$, but is less directly comparable due to the different ρ threshold for the Dec-
700 can swarm.

701 The median length of Deccan clusters (~ 93 km) is significantly longer ($3x$) than
702 the CRBG clusters (~ 29 km). Comparing the eruptive volume and median length we
703 see similar ratios of $11km^2$ and $7km^2$. The median width of Deccan clusters (~ 2 km)
704 is larger than the CRBG clusters (~ 0.7 km). Although this difference might be attributed
705 to the ρ thresholds based on segment mean length between the CFBs, we note that sim-
706 ilar widths arise if a comparable ρ threshold had been used for the CRBG (See Supple-
707 ment). The median cluster aspect ratios are similar 53 vs 48 for the Deccan and CRBG
708 respectively (Figure 4.3.5D). The similar aspect ratios implies that the dike emplacement
709 mechanics are the same for both swarms despite the significantly longer clustered dikes
710 in the Deccan. Finally, the amount of estimated maximum strain is similar for both swarms
711 despite their difference in spatial area.

712 Together, these similarities between clustered dike segments, in the context of erupted
713 volume ratios between CRBG and Deccan, suggest that spatial patterns of LIP magmatic
714 geometry scales with total eruptive output. Such structural similarities, measured both
715 on province scale and via dike cluster sizes, are remarkable. Although two examples is
716 hardly a robust trend, the implications are interesting and unexpected given significant
717 differences in other aspects of the CFBs. We can also roughly extend this to the Span-
718 ish Peaks although the different geologic setting and unknown volumes make direct com-
719 parisons difficult. We use the swarm centered on West Peak, which may represent the
720 scale of a typical long-lived volcanic center and paleo-edifice (Harp, 2021), to examine
721 the scaling between area and number of dikes to CFBs. We use an estimated “erupted”
722 volume for West Peak based on averages of volcanic complexes compiled in O’Hara et
723 al. (2020) and Grosse et al. (2009). Extending the scaling trend to West Peak over es-
724 timates the erupted volume and area by up to two orders of magnitude however the com-
725 parison between the West Peak and the voluminous LIP datasets is difficult to make es-
726 pecially considering the high uncertainty on the West Peak eruptive system.

727 If erupted volumes are imprinted on the spatial structure of the transcrustal magma
728 transport system, this scaling provides a tool for connecting surface volcanic expression
729 to deep transport that is hidden from view. Conversely, it is also of interest to connect

730 exhumed transport systems, for example plutonic systems (Karlstrom et al., 2017), an-
731 cient dike swarms (Fahrig & Jones, 1969; Baragar et al., 1996), or planetary examples
732 (Ernst et al., 1995), to active processes.

733 5 Conclusion

734 We have developed a tool based on the Hough Transform for objective extraction
735 of structures in complex distributions of quasi-linear segments, such as are prevalent in
736 terrestrial dike swarms. We have tested this tool with synthetic data and applied it to
737 three dike swarms, associated with the Spanish Peaks, Colorado, USA, the Columbia River
738 Flood Basalts, USA, and the Deccan Traps, India. We found that dike segments can be
739 linked together into aligned structures that may represent dikes or packets of highly clus-
740 tered dikes. Looking at the linked datasets we find significantly longer sustained struc-
741 tures which average 30 km in CFBs and can reach well over 200 km. The Hough Trans-
742 form also facilitates investigation of dike swarm mesoscale structure in two end mem-
743 bers: linear and radial patterns. Firstly, we do not find that a single radial center is well
744 fit by the dike data in any of the three provinces. However, we do find that the dike swarms
745 can be decomposed into smaller localized radial patterns which may represent rotating
746 stress fields over time or the influence of an isotropic stress field.

747 For CFBs, the apparent generality of structures and scaling provide a template for
748 future study both of the CRBG and Deccan as well as other flood basalt systems. We
749 expect that future work incorporating compositions (Reidel, Camp, Tolan, & Martin,
750 2013), paleomagnetic polarity (Biasi & Karlstrom, 2021), and direct geochronology (Kasbohm
751 & Schoene, 2018; Fendley et al., 2019; Schoene et al., 2021; H. Sheth et al., 2019) will
752 be necessary to robustly link individual segments together. Additional statistical char-
753 acterization, such as analysis of the dendrogram generated via the hierarchical cluster-
754 ing methods (Jarman, 2020), could seek to establish the range of mesoscale structures
755 that exist. Additionally, the Hough transform method could be generalized to include
756 curvilinear segments, which are not uncommon in dike swarms but neglected here for sim-
757 plicity. This method as described here which we applied to dike swarms could also be
758 applied to many types of linear/curved structures including fracture sets, fault networks,
759 and shear zones on Earth or on other planets.

Open Research Section

The data sets generated by our linking method are available in the supplement. The code used to create those data sets and figures in the paper are available for inspection and citation at [10.5281/zenodo.7415877](https://doi.org/10.5281/zenodo.7415877).

Acknowledgments

The authors thank Chris Harper for his insightful discussion in developing this method and the 2020 and 2021 Columbia River Flood Basalts reading group organized by Leif Karlstrom with special thanks to Emily Cahoon, Dylan Patrick Colon, Maria McQuillan, and Mary Mass who were part of the initial work on this project. TM acknowledges support by the MIT Crosby Postdoctoral Fellowship. LK acknowledges NSF grant 1848554.

References

- Acocella, V., & Neri, M. (2009). Dike propagation in volcanic edifices: Overview and possible developments. *Tectonophysics*, *471*(1-2), 67–77. doi: 10.1016/j.tecto.2008.10.002
- Ayele, A., Jacques, E., Kassim, M., Kidane, T., Omar, A., Tait, S., . . . King, G. (2007). The volcano-seismic crisis in Afar, Ethiopia, starting September 2005. *Earth and Planetary Science Letters*, *255*(1-2), 177–187. doi: 10.1016/j.epsl.2006.12.014
- Babiker, M., & Gudmundsson, A. (2004). Geometry, structure and emplacement of mafic dykes in the Red Sea Hills, Sudan. *Journal of African Earth Sciences*, *38*(3), 279–292. doi: 10.1016/j.jafrearsci.2004.01.003
- Ballard, D. H. (1981). Generalizing the Hough transform to detect arbitrary shapes. *Pattern Recognition*, *13*(2), 111–122. doi: 10.1016/0031-3203(81)90009-1
- Baragar, W. R., Ernst, R. E., Hulbert, L., & Peterson, T. (1996). Longitudinal petrochemical variation in the Mackenzie dyke swarm, Northwestern Canadian shield. *Journal of Petrology*, *37*(2), 317–359. doi: 10.1093/petrology/37.2.317
- Bhattacharji, S., Chatterjee, N., Wampler, J. M., Nayak, P. N., & Deshmukh, S. S. (1996). Indian intraplate and continental margin rifting, lithospheric extension, and mantle upwelling in deccan flood basalt volcanism near the K/T boundary: Evidence from mafic dike swarms. *Journal of Geology*, *104*(4), 379–398. doi: 10.1086/629835

- 791 Biasi, J., & Karlstrom, L. (2021). Timescales of magma transport in the Columbia
792 River flood basalts, determined by paleomagnetic data. *Earth and Planetary
793 Science Letters*, 576, 117169. Retrieved from [https://doi.org/10.1016/
794 j.epsl.2021.117169](https://doi.org/10.1016/j.epsl.2021.117169) doi: 10.1016/j.epsl.2021.117169
- 795 Black, B. A., Karlstrom, L., & Mather, T. A. (2021). The life cycle of large igneous
796 provinces. *Nature Reviews Earth and Environment*, 2(12), 840–857. doi: 10
797 .1038/s43017-021-00221-4
- 798 Blakely, R. J., Sherrod, B. L., Weaver, C. S., Wells, R. E., & Rohay, A. C. (2014,
799 6). The Wallula fault and tectonic framework of south-central Washington, as
800 interpreted from magnetic and gravity anomalies. *Tectonophysics*, 624–625,
801 32–45. doi: 10.1016/j.tecto.2013.11.006
- 802 Bond, D. P., & Wignall, P. B. (2014). Large igneous provinces and mass extinctions:
803 An update. *Special Paper of the Geological Society of America*, 505(December
804 2015), 29–55. doi: 10.1130/2014.2505(02)
- 805 Bungler, A. P., Menand, T., Cruden, A., Zhang, X., & Halls, H. (2013). Analytical
806 predictions for a natural spacing within dyke swarms. *Earth and Planetary
807 Science Letters*, 375, 270–279. doi: 10.1016/j.epsl.2013.05.044
- 808 Bungler, A. P., Zhang, X., & Jeffrey, R. G. (2012). Parameters affecting the inter-
809 action among closely spaced hydraulic fractures. *SPE Journal*, 17(1), 292–306.
810 doi: 10.2118/140426-PA
- 811 Cahoon, E. B., Streck, M. J., Koppers, A. A., & Miggins, D. P. (2020). Reshuffling
812 the columbia river basalt chronology—picture gorge basalt, the earliest-and
813 longest-erupting formation. *Geology*, 48(4), 348–352.
- 814 Callot, J. P., Geoffroy, L., Aubourg, C., Pozzi, J. P., & Mege, D. (2001). Magma
815 flow directions of shallow dykes from the East Greenland volcanic margin in-
816 ferred from magnetic fabric studies. *Tectonophysics*, 335(3-4), 313–329. doi:
817 10.1016/S0040-1951(01)00060-9
- 818 Camp, V., Reidel, S., Ross, M., Brown, R., & Self, S. (2017). Field-Trip Guide to
819 the Vents , Dikes , Stratigraphy , and Structure of the Columbia River Basalt
820 Group , Eastern Oregon and Southeastern Washington. *Scientific Investiga-
821 tions Report 2017-5022-N*(October), 88 p. doi: 10.3133/sir20175022N
- 822 Camp, V. E., & Ross, M. E. (2004). Mantle dynamics and genesis of mafic magma-
823 tism in the intermontane Pacific Northwest. *Journal of Geophysical Research*:

- 824 *Solid Earth*, 109(8), 1–14. doi: 10.1029/2003JB002838
- 825 Crane, K., & Bohanon, A. (2021). Dike Propagation During Global Contraction:
826 Making Sense of Conflicting Stress Histories on Mercury. *Frontiers in Earth*
827 *Science*, 9(December), 1–14. doi: 10.3389/feart.2021.752864
- 828 Davis, T., Bagnardi, M., Lundgren, P., & Rivalta, E. (2021). Extreme Curvature
829 of Shallow Magma Pathways Controlled by Competing Stresses: Insights From
830 the 2018 Sierra Negra Eruption. *Geophysical Research Letters*, 48(13), 1–10.
831 doi: 10.1029/2021GL093038
- 832 Delaney, P. T., Pollard, D. D., Ziony, J. I., & McKee, E. H. (1986). Field re-
833 lations between dikes and joints: Emplacement processes and paleostress
834 analysis. *Journal of Geophysical Research*, 91(B5), 4920. doi: 10.1029/
835 jb091ib05p04920
- 836 Dole, G., Das, S., & Kale, V. S. (2022). Tectonic framework of geomorphic evolution
837 of the deccan volcanic province, india. *Earth-Science Reviews*, 228, 103988.
- 838 Duda, R. O., & Hart, P. E. (1972). Use of the Hough Transformation to Detect
839 Lines and Curves in Pictures. *Communications of the ACM*, 15(1), 11–15. doi:
840 10.1145/361237.361242
- 841 Eberhardt, E. (2012). The hoek–brown failure criterion. In *The isrm suggested*
842 *methods for rock characterization, testing and monitoring: 2007-2014* (pp.
843 233–240). Springer.
- 844 Ernst, R. E., Bond, D. P. G., Zhang, S., Buchan, K. L., Grasby, S. E., Youbi, N.,
845 ... Doucet, L. S. (2021). Large Igneous Province Record Through Time and
846 Implications for Secular Environmental Changes and Geological Time-Scale
847 Boundaries. (January), 1–26. doi: 10.1002/9781119507444.ch1
- 848 Ernst, R. E., & Buchan, K. L. (1997). Giant radiating dyke swarms: Their use in
849 identifying pre-Mesozoic large igneous provinces and mantle plumes. *Geophysi-*
850 *cal Monograph Series*, 100, 297–333. doi: 10.1029/GM100p0297
- 851 Ernst, R. E., Grosfils, E. B., & Mege, D. (2001). Giant Dike Swarms: Earth , Venus
852 , and Mars. *Annu. Rev. Earth Planetary Science*(29), 489–534.
- 853 Ernst, R. E., Head, J. W., Parfitt, E., Grosfils, E., & Wilson, L. (1995). Giant radi-
854 ating dyke swarms on Earth and Venus. *Earth Science Reviews*, 39(1-2), 1–58.
855 doi: 10.1016/0012-8252(95)00017-5
- 856 Everitt, B. (1980). *Cluster analysis* (Vol. 14) (No. 1). doi: 10.1007/BF00154794

- 857 Fahrig, W. F., & Jones, D. L. (1969). Paleomagnetic evidence for the extent of
 858 Mackenzie igneous events. *Canadian Journal of Earth Sciences*, *6*(4), 679–688.
 859 doi: 10.1139/e69-065
- 860 Fendley, I. M., Mittal, T., Sprain, C. J., Marvin-DiPasquale, M., Tobin, T. S.,
 861 & Renne, P. R. (2019). Constraints on the volume and rate of Deccan
 862 Traps flood basalt eruptions using a combination of high-resolution terres-
 863 trial mercury records and geochemical box models. *Earth and Planetary*
 864 *Science Letters*, *524*, 115721. Retrieved from [https://doi.org/10.1016/](https://doi.org/10.1016/j.epsl.2019.115721)
 865 [j.epsl.2019.115721](https://doi.org/10.1016/j.epsl.2019.115721) doi: 10.1016/j.epsl.2019.115721
- 866 Fruchter, J. S., & Baldwin, S. F. (1975). Correlations between dikes of the monu-
 867 ment swarm, central oregon, and picture gorge basalt flows. *Geological Society*
 868 *of America Bulletin*, *86*(4), 514–516.
- 869 Glazner, A. F., & Mills, R. D. (2012). Interpreting two-dimensional cuts through
 870 broken geologic objects: Fractal and non-fractal size distributions. *Geosphere*,
 871 *8*(4), 902–914. doi: 10.1130/GES00731.1
- 872 Glen, J. M., & Ponce, D. A. (2002). Large-scale fractures related to inception of the
 873 Yellowstone hotspot. *Geology*, *30*(7), 647–650. doi: 10.1130/0091-7613(2002)
 874 030<0647:LSFRTI>2.0.CO;2
- 875 Gonnermann, H., & Taisne, B. (2015). Magma Transport in Dikes Author 's per-
 876 sonal copy. *Encyclopedia of Volcanoes*, 215–224.
- 877 Grosfils, E. B., & Head, J. W. (1994). Emplacement of a Radiating Dike Swarm in
 878 Western Vinmara Planitia, Venus: Interpretation of the Regional Stress Field
 879 Orientation and Subsurface Magmatic Configuration.
- 880 Grosse, P., van Wyk de Vries, B., Petrinovic, I. A., Euillades, P. A., & Alvarado,
 881 G. E. (2009). Morphometry and evolution of arc volcanoes. *Geology*, *37*(7),
 882 651–654. doi: 10.1130/G25734A.1
- 883 GSI District Resource Map. (2001). *District Resource Maps - India* (Tech. Rep.).
 884 GSI Bhukosh. (2020 (accessed December 1, 2020)). Bhukosh [Computer software
 885 manual]. Retrieved from [\url{http://bhukosh.gsi.gov.in/}](http://bhukosh.gsi.gov.in/)
- 886 Gudmundsson, A. (1995). Infrastructure and mechanics of volcanic systems in Ice-
 887 land. *Journal of Volcanology and Geothermal Research*, *64*(1-2), 1–22. doi: 10
 888 .1016/0377-0273(95)92782-Q
- 889 Gudmundsson, A. (2002). Emplacement and arrest of sheets and dykes in cen-

- 890 tral volcanoes. *Journal of Volcanology and Geothermal Research*, 116(3-4),
891 279–298. doi: 10.1016/S0377-0273(02)00226-3
- 892 Gudmundsson, A. (2006). How local stresses control magma-chamber ruptures, dyke
893 injections, and eruptions in composite volcanoes. *Earth-Science Reviews*, 79(1-
894 2), 1–31. doi: 10.1016/j.earscirev.2006.06.006
- 895 Gunaydin, D., Peirce, A. P., & Bungler, A. P. (2021, 1). Laboratory Exper-
896 iments Contrasting Growth of Uniformly and Nonuniformly Spaced Hy-
897 draulic Fractures. *Journal of Geophysical Research: Solid Earth*, 126(1).
898 Retrieved from [https://onlinelibrary.wiley.com/doi/full/10.1029/](https://onlinelibrary.wiley.com/doi/full/10.1029/2020JB020107)
899 [https://onlinelibrary.wiley.com/doi/abs/10.1029/](https://onlinelibrary.wiley.com/doi/abs/10.1029/2020JB020107)
900 [https://agupubs.onlinelibrary.wiley.com/doi/10.1029/](https://agupubs.onlinelibrary.wiley.com/doi/10.1029/2020JB020107)
901 [2020JB020107](https://doi.org/10.1029/2020JB020107) doi: 10.1029/2020JB020107
- 902 Harp, A. G. (2021). Magma propagation and emplacement within the central intru-
903 sive complex of Summer Coon stratovolcano, Colorado. *Journal of Volcanology*
904 *and Geothermal Research*, 419, 107372. Retrieved from [https://doi.org/10](https://doi.org/10.1016/j.jvolgeores.2021.107372)
905 [.1016/j.jvolgeores.2021.107372](https://doi.org/10.1016/j.jvolgeores.2021.107372) doi: 10.1016/j.jvolgeores.2021.107372
- 906 Hough, P. V. C. (1962). *A method and means for recognition complex patterns*.
- 907 Jarman, A. M. (2020). Hierarchical Cluster Analysis: Comparison of Single link-
908 age, Complete linkage, Average linkage and Centroid Linkage Method. , 1–13.
909 Retrieved from [https://www.researchgate.net/publication/339443595](https://www.researchgate.net/publication/339443595_Hierarchical_Cluster_Analysis_Comparison_of_Single_linkage_Complete_linkage_Average_linkage_and_Centroid_Linkage_Method)
910 [_Hierarchical_Cluster_Analysis_Comparison_of_Single_linkage_Complete](https://www.researchgate.net/publication/339443595_Hierarchical_Cluster_Analysis_Comparison_of_Single_linkage_Complete_linkage_Average_linkage_and_Centroid_Linkage_Method)
911 [_linkage_Average_linkage_and_Centroid_Linkage_Method](https://www.researchgate.net/publication/339443595_Hierarchical_Cluster_Analysis_Comparison_of_Single_linkage_Complete_linkage_Average_linkage_and_Centroid_Linkage_Method)
- 912 Jay, A. E., & Widdowson, M. (2008). Stratigraphy, structure and volcanology of
913 the SE Deccan continental flood basalt province: Implications for eruptive
914 extent and volumes. *Journal of the Geological Society*, 165(1), 177–188. doi:
915 10.1144/0016-76492006-062
- 916 John, D. U. G. S., Wallace, A. U. G. S., Ponce, D., Fleck, R., & Conrad, J. (2000).
917 New Perspectives on the Geology and Origin of the Northern Nevada Rift..
- 918 Johnson, R. (1961). Patterns and Origin of Radial Dike Swarms Associated with
919 West Spanish Peak and Dike Mountain, South-Central Colorado. *Geological*
920 *Society of America Bulletin*, 72(April), 579–590.
- 921 Jolly, R. J., & Sanderson, D. J. (1995). Variation in the form and distribution of
922 dykes in the Mull swarm, Scotland. *Journal of Structural Geology*, 17(11),

- 923 1543–1557. doi: 10.1016/0191-8141(95)00046-G
- 924 Karlstrom, L., Dufek, J., & Manga, M. (2009). Organization of volcanic
925 plumbing through magmatic lensing by magma chambers and volcanic
926 loads. *Journal of Geophysical Research: Solid Earth*, *114*(10), 1–16. doi:
927 10.1029/2009JB006339
- 928 Karlstrom, L., Paterson, S. R., & Jellinek, A. M. (2017). A reverse energy cascade
929 for crustal magma transport. *Nature Geoscience*, *10*(8), 604–608. doi: 10
930 .1038/NGEO2982
- 931 Kasbohm, J., & Schoene, B. (2018, 9). Rapid eruption of the Columbia River flood
932 basalt and correlation with the mid-Miocene climate optimum. *Science Ad-
933 vances*, *4*(9), 8223. Retrieved from [https://www.science.org/doi/10.1126/
934 sciadv.aat8223](https://www.science.org/doi/10.1126/sciadv.aat8223) doi: 10.1126/SCIADV.AAT8223/SUPPL{\-}FILE/
935 AAT8223{\-}TABLE{\-}S1.XLS
- 936 Kavanagh, J., & Pavier, M. (2014). Rock interface strength influences fluid-filled
937 fracture propagation pathways in the crust. *Journal of Structural Geology*, *63*,
938 68–75.
- 939 Kavanagh, J. L., Boutelier, D., & Cruden, A. R. (2015). The mechanics of sill in-
940 ception, propagation and growth: Experimental evidence for rapid reduction
941 in magmatic overpressure. *Earth and Planetary Science Letters*, *421*, 117–128.
942 doi: 10.1016/j.epsl.2015.03.038
- 943 Kavanagh, J. L., Burns, A. J., Hilmi Hazim, S., Wood, E. P., Martin, S. A., Hignett,
944 S., & Dennis, D. J. (2018). Challenging dyke ascent models using novel labo-
945 ratory experiments: Implications for reinterpreting evidence of magma ascent
946 and volcanism. *Journal of Volcanology and Geothermal Research*, *354*, 87–101.
947 Retrieved from <https://doi.org/10.1016/j.jvolgeores.2018.01.002> doi:
948 10.1016/j.jvolgeores.2018.01.002
- 949 Kavanagh, J. L., Menand, T., & Sparks, R. S. J. (2006). An experimental inves-
950 tigation of sill formation and propagation in layered elastic media. *Earth and
951 Planetary Science Letters*, *245*(3-4), 799–813. doi: 10.1016/j.epsl.2006.03.025
- 952 Krumbholz, M., Hieronymus, C. F., Burchardt, S., Troll, V. R., Tanner, D. C., &
953 Friese, N. (2014). Weibull-distributed dyke thickness reflects probabilis-
954 tic character of host-rock strength. *Nature Communications*, *5*, 1–7. doi:
955 10.1038/ncomms4272

- 956 Ma, L., Li, Z., Wang, M., Wu, J., & Li, G. (2020). Applicability of a new modified
 957 explicit three-dimensional hoek-brown failure criterion to eight rocks. *International Journal of Rock Mechanics and Mining Sciences*, *133*, 104311.
 958
- 959 McKinney, W., et al. (2011). pandas: a foundational python library for data analysis
 960 and statistics. *Python for high performance and scientific computing*, *14*(9), 1–
 961 9.
- 962 Mège, D., & Korme, T. (2004, 5). Dyke swarm emplacement in the Ethiopian Large
 963 Igneous Province: Not only a matter of stress. *Journal of Volcanology and
 964 Geothermal Research*, *132*(4), 283–310. doi: 10.1016/S0377-0273(03)00318-4
- 965 Mittal, T., & Richards, M. A. (2021). The Magmatic Architecture of Continental
 966 Flood Basalts: 2. A New Conceptual Model. *Journal of Geophysical Research:
 967 Solid Earth*, *126*(12). doi: 10.1029/2021JB021807
- 968 Mittal, T., Richards, M. A., & Fendley, I. M. (2021). The Magmatic Architecture of
 969 Continental Flood Basalts I: Observations From the Deccan Traps. *Journal of
 970 Geophysical Research: Solid Earth*, *126*(12), 1–81. doi: 10.1029/2021jb021808
- 971 Morriss, M. C., Karlstrom, L., Nasholds, M. W., & Wolff, J. A. (2020). The
 972 chief Joseph dike swarm of the Columbia river flood basalts, and the legacy
 973 data set of William H. Taubeneck. *Geosphere*, *16*(4), 1793–1817. doi:
 974 10.1130/GES02173.1
- 975 Muller, O. H., & Pollard, D. D. (1977). The stress state near Spanish Peaks,
 976 colorado determined from a dike pattern. *Pure and Applied Geophysics PA-
 977 GEOPH*, *115*(1-2), 69–86. doi: 10.1007/BF01637098
- 978 Müllner, D. (2011). Modern hierarchical, agglomerative clustering algorithms.
 979 (1973), 1–29. Retrieved from <http://arxiv.org/abs/1109.2378>
- 980 Odé, H. (1957). Mechanical analysis of the dike pattern of the Spanish peaks area,
 981 Colorado. *Bulletin of the Geological Society of America*, *68*(5), 567–576. doi:
 982 10.1130/0016-7606(1957)68[567:MAOTDP]2.0.CO;2
- 983 O’Hara, D., Karlstrom, L., & Ramsey, D. W. (2020, 7). Time-evolving surface and
 984 subsurface signatures of Quaternary volcanism in the Cascades arc. *Geology*,
 985 *48*(11), 1088–1093. Retrieved from <https://doi.org/10.1130/G47706.1> doi:
 986 10.1130/G47706.1
- 987 pandas development team, T. (2020, 2). *pandas-dev/pandas: Pandas*. Zenodo.
 988 Retrieved from <https://doi.org/10.5281/zenodo.3509134> doi: 10.5281/

989 zenodo.3509134

- 990 Paquet, F., Dauteuil, O., Hallot, E., & Moreau, F. (2007). Tectonics and magma
 991 dynamics coupling in a dyke swarm of Iceland. *Journal of Structural Geology*,
 992 *29*(9), 1477–1493. doi: 10.1016/j.jsg.2007.06.001
- 993 Penn, B. S., & Lindsey, D. A. (2009). 40Ar/39Ar dates for the Spanish Peaks intru-
 994 sions in south-central Colorado. *Rocky Mountain Geology*, *44*(1), 17–32. doi:
 995 10.2113/gsrocky.44.1.17
- 996 Petcovic, H., & Grunder, A. (2003). Textural and thermal history of partial melting
 997 in tonalitic wallrock at the margin of a basalt dike, wallowa mountains, oregon.
 998 *Journal of Petrology*, *44*(12), 2287–2312.
- 999 Petcovic, H. L., & Dufek, J. D. (2005). Modeling magma flow and cooling in dikes:
 1000 Implications for emplacement of Columbia River flood basalts. *Journal of Geo-*
 1001 *physical Research: Solid Earth*, *110*(10), 1–15. doi: 10.1029/2004JB003432
- 1002 Pollard, D. D., Segall, P., & Delaney, P. T. (1982). Formation and interpretation of
 1003 dilatant echelon cracks. *Geological Society of America Bulletin*, *93*(12), 1291–
 1004 1303. doi: 10.1130/0016-7606(1982)93<1291:FAIODE>2.0.CO;2
- 1005 Rajaram, M., Anand, S., Erram, V. C., & Shinde, B. (2017). Insight into the
 1006 structures below the deccan trap-covered region of maharashtra, india from
 1007 geopotential data. *Geological Society, London, Special Publications*, *445*(1),
 1008 219–236.
- 1009 Rao, J., Ravikumar, B., & Golani, P. R. (2022). What lies beneath the deccan
 1010 volcanic province? perspective on tectonic elements and sub-trappean geology
 1011 from gravity signatures. *Journal of Earth System Science*, *131*(1), 1–20.
- 1012 Ray, R., Sheth, H. C., & Mallik, J. (2007). Structure and emplacement of the
 1013 Nandurbar-Dhule mafic dyke swarm, Deccan Traps, and the tectonomagmatic
 1014 evolution of flood basalts. *Bulletin of Volcanology*, *69*(5), 537–551. doi:
 1015 10.1007/s00445-006-0089-y
- 1016 Reidel, S. P., Camp, V. E., Tolan, T. L., Kauffman, J. D., & Garwood, D. L. (2013).
 1017 Tectonic evolution of the Columbia River flood basalt province. *Special Paper*
 1018 *of the Geological Society of America*, *497*(August), 293–324. doi: 10.1130/2013
 1019 .2497(12)
- 1020 Reidel, S. P., Camp, V. E., Tolan, T. L., & Martin, B. S. (2013). The Columbia
 1021 River flood basalt province: Stratigraphy, areal extent, volume, and physical

- 1022 volcanology. *Special Paper of the Geological Society of America*, 497, 1–43.
 1023 doi: 10.1130/2013.2497(01)
- 1024 Rivalta, E., Taisne, B., Bungler, A. P., & Katz, R. F. (2015). A review of mechanical
 1025 models of dike propagation: Schools of thought, results and future directions.
 1026 *Tectonophysics*, 638(C), 1–42. doi: 10.1016/j.tecto.2014.10.003
- 1027 Rivas-Dorado, S., Ruíz, J., & Romeo, I. (2022, 9). Giant dikes and dike-induced seis-
 1028 micity in a weak crust underneath Cerberus Fossae, Mars. *Earth and Planetary
 1029 Science Letters*, 594, 117692. doi: 10.1016/J.EPSL.2022.117692
- 1030 Roman, A., & Jaupart, C. (2014). The impact of a volcanic edifice on intrusive and
 1031 eruptive activity. *Earth and Planetary Science Letters*, 408, 1–8. Retrieved
 1032 from <http://dx.doi.org/10.1016/j.epsl.2014.09.016> doi: 10.1016/j.epsl
 1033 .2014.09.016
- 1034 Rubin, A. M. (1995). Propagation of Magma-filled Cracks. *Annual Review of Earth
 1035 & Planetary Sciences*, 287–336.
- 1036 Schoene, B., Eddy, M. P., Keller, C. B., & Samperton, K. M. (2021). An evalua-
 1037 tion of Deccan Traps eruption rates using geochronologic data. *Geochronology*,
 1038 3(1), 181–198. doi: 10.5194/gchron-3-181-2021
- 1039 Self, S., Mittal, T., Dole, G., & Vanderkluysen, L. (2022a). Toward Understand-
 1040 ing Deccan Volcanism. *Annual Review of Earth and Planetary Sciences*, 50(1),
 1041 477–506. Retrieved from <https://doi.org/10.1146/annurev-earth-012721-051416>
 1042 doi: 10.1146/annurev-earth-012721-051416
- 1043 Self, S., Mittal, T., Dole, G., & Vanderkluysen, L. (2022b). Toward understanding
 1044 deccan volcanism. *Annual Review of Earth and Planetary Sciences*, 50, 477–
 1045 506.
- 1046 Sheth, H., Vanderkluysen, L., Demonterova, E. I., Ivanov, A. V., & Savatenkov,
 1047 V. M. (2019). Geochemistry and $^{40}\text{Ar}/^{39}\text{Ar}$ geochronology of the
 1048 Nandurbar-Dhule mafic dyke swarm: Dyke-sill-flow correlations and strati-
 1049 graphic development across the Deccan flood basalt province. *Geological
 1050 Journal*, 54(1), 157–176. doi: 10.1002/gj.3167
- 1051 Sheth, H. C., & Cañón-Tapia, E. (2015). Are flood basalt eruptions monogenetic or
 1052 polygenetic? *International Journal of Earth Sciences*, 104(8), 2147–2162. Re-
 1053 trieved from <http://dx.doi.org/10.1007/s00531-014-1048-z> doi: 10.1007/
 1054 s00531-014-1048-z

- 1055 Shukla, G., Mallik, J., & Mondal, P. (2022, 11). Dimension-scaling relationships of
 1056 Pachmarhi dyke swarm and their implications on Deccan magma emplacement.
 1057 *Tectonophysics*, *843*, 229602. doi: 10.1016/J.TECTO.2022.229602
- 1058 SNEATH, P. H. (1957, 8). The application of computers to taxonomy. *Jour-*
 1059 *nal of general microbiology*, *17*(1), 201–226. Retrieved from [https://](https://www.microbiologyresearch.org/content/journal/micro/10.1099/00221287-17-1-201)
 1060 [www.microbiologyresearch.org/content/journal/micro/10.1099/](https://www.microbiologyresearch.org/content/journal/micro/10.1099/00221287-17-1-201)
 1061 [00221287-17-1-201](https://www.microbiologyresearch.org/content/journal/micro/10.1099/00221287-17-1-201) doi: 10.1099/00221287-17-1-201/CITE/REFWORKS
- 1062 Sorenson, T. (1948). A method of establishing groups of equal amplitude in plant
 1063 sociology based on similarity of species content and its application to analyses
 1064 of the vegetation on Danish commons. *Biologiske Skrifter*, *5*, 1–34.
- 1065 Thiele, S. T., Cruden, A. R., Micklethwaite, S., Bunger, A. P., & Köpping, J.
 1066 (2020). Dyke apertures record stress accumulation during sustained volcanism.
 1067 *Scientific Reports*, *10*(1), 1–9. Retrieved from [https://doi.org/10.1038/](https://doi.org/10.1038/s41598-020-74361-w)
 1068 [s41598-020-74361-w](https://doi.org/10.1038/s41598-020-74361-w) doi: 10.1038/s41598-020-74361-w
- 1069 Townsend, M., & Huber, C. (2020). A critical magma chamber size for volcanic
 1070 eruptions. *Geology*, *48*(5), 431–435. doi: 10.1130/G47045.1
- 1071 Urbani, S., Acocella, V., & Rivalta, E. (2018). What Drives the Lateral
 1072 Versus Vertical Propagation of Dikes? Insights From Analogue Models.
 1073 *Journal of Geophysical Research: Solid Earth*, *123*(5), 3680–3697. doi:
 1074 [10.1029/2017JB015376](https://doi.org/10.1029/2017JB015376)
- 1075 Vanderkluysen, L., Mahoney, J. J., Hooper, P. R., Sheth, H. C., & Ray, R. (2011).
 1076 The feeder system of the Deccan Traps (India): Insights from dike geochem-
 1077 istry. *Journal of Petrology*, *52*(2), 315–343. doi: 10.1093/petrology/egq082
- 1078 Virtanen, P., Gommers, R., Oliphant, T. E., Haberland, M., Reddy, T., Cournapeau,
 1079 D., . . . Contributors, S. . (2020). SciPy 1.0: Fundamental Algorithms for
 1080 Scientific Computing in Python. *Nature Methods*, *17*, 261–272.
- 1081 Wadge, G., Biggs, J., Lloyd, R., & Kendall, J. M. (2016). Historical volcanism and
 1082 the state of stress in the east African rift system. *Frontiers in Earth Science*,
 1083 *4*(September). doi: 10.3389/feart.2016.00086
- 1084 Wolff, J. A., Ramos, F. C., Hart, G. L., Patterson, J. D., & Brandon, A. D. (2008).
 1085 Columbia River flood basalts from a centralized crustal magmatic sys-
 1086 tem. *Nature Geoscience*, *1*(3), 177–180. Retrieved from [www.nature.com/](http://www.nature.com/naturegeoscience)
 1087 [naturegeoscience](http://www.nature.com/naturegeoscience) doi: 10.1038/ngeo124

- 1088 Yale, L. B., & Carpenter, S. J. (1998). Large igneous provinces and giant
1089 dike swarms: Proxies for supercontinent cyclicality and mantle convec-
1090 tion. *Earth and Planetary Science Letters*, 163(1-4), 109–122. doi:
1091 10.1016/S0012-821X(98)00179-4
- 1092 Ziou, D., & Tabbone, S. (1998). Edge detection techniques - an overview. *Pria*,
1093 1–41. Retrieved from [http://nyx-www.informatik.uni-bremen.de/1044/1/](http://nyx-www.informatik.uni-bremen.de/1044/1/ziou_pria_98.pdf)
1094 [ziou_pria_98.pdf](http://nyx-www.informatik.uni-bremen.de/1044/1/ziou_pria_98.pdf)